water

MDPI

Article

Evolution Process of Ancient Landslide Reactivation under the Action of Rainfall: Insights from Model Tests

Xiang Li [1,2], Ruian Wu [1,3,*], Bing Han [4,*], Deguang Song [1,5], Zhongkang Wu [1,2], Wenbo Zhao [1,2] and Qijun Zou [1,2]

[1] Institute of Geomechanics, Chinese Academy of Geological Sciences, Beijing 100081, China; lix1228@cug.edu.cn (X.L.)
[2] School of Engineering, China University of Geosciences (Wuhan), Wuhan 430074, China
[3] Key Laboratory of Active Tectonics and Geological Safety, Ministry of Natural Resources, Beijing 100081, China
[4] China Institute for Geo-Environment Monitoring, Beijing 100081, China
[5] Yunnan Geological Engineering Second Survey Institute Co., Ltd., Kunming 650218, China
* Correspondence: wuruian1991@126.com (R.W.); hanbing@mail.cgs.gov.cn (B.H.)

Abstract: Under rapid global climate change, the risk of ancient landslide reactivation induced by rainfall infiltration is increasing significantly. The contribution of cracks to the reactivation of ancient landslides, as an evolutionary product, is a topic that deserves attention; however, current research on this issue remains insufficient. In this study, taking the Woda landslide in the upper Jinsha River as a case study, we investigated the reactivation mechanisms of ancient landslides with and without cracks under rainfall based on model tests. The study showed that cracks influence the reactivation range and depth of ancient landslide. In cases where no cracks develop on ancient landslides, rainfall can only cause shallow sliding with failure concentrated at its front edge. Conversely, when cracks develop on ancient landslides, rainwater can quickly infiltrate into the sliding zone along the cracks and induce overall reactivation of the ancient landslide. Furthermore, the reactivation mechanism of ancient landslides without cracks is that the failure of ancient landslide foot results in progressive failure at the front of the ancient landslide. When cracks have developed at ancient landslides, the reactivation mechanism of which involves mid-rear ancient landslide creeping, tensile cracks develop on the mid-rear ancient landslide, with localized sliding at the front edge, tensile cracks extending, local sliding range extending, accelerated creeping, and progressive failure of the mid-rear ancient landslide. These findings shed light on how cracks influence rainfall-induced mechanisms of ancient landslide reactivation and hold great significance for advancing our understanding regarding these mechanisms.

Keywords: ancient landslide; reactivation mechanism; rainfall; crack; model test

Citation: Li, X.; Wu, R.; Han, B.; Song, D.; Wu, Z.; Zhao, W.; Zou, Q. Evolution Process of Ancient Landslide Reactivation under the Action of Rainfall: Insights from Model Tests. *Water* **2024**, *16*, 583. https://doi.org/10.3390/w16040583

Academic Editor: Renato Morbidelli

Received: 22 January 2024
Revised: 10 February 2024
Accepted: 12 February 2024
Published: 16 February 2024

1. Introduction

The technical term "paleo-landslide" typically refers to landslides that have been formed for a relatively long time, the classification of which has been subject to varying perspectives [1–5]. In engineering geological practice, considerable attention is given to the present stability status of ancient landslides. With the increasing intensity of human activities and the frequent occurrence of extreme conditions such as strong earthquakes and heavy rainfall, the risk of ancient landslide reactivation has sharply risen, severely constraining human engineering programming and construction and causing significant losses to the lives and properties of local people [6–9]. For example, in 2014, under the combined actions of excavation at the foot of the landslide, Thompson River erosion, and heavy rainfall near the ancient landslide group in the Thompson River valley, Canada's national railway (CN and CP) reactivated, severely affecting the operational safety of the railway [10]. In 2016, extreme rainfall caused multiple ancient landslides to reactivate in the

upstream area of the Tanarello River, Italy, resulting in the destruction of buildings and highways [9]. In July 2018, continuous heavy rainfall induced the reactivation of the Jiangdingya ancient landslide in Zhouqu County, Gansu Province, China, blocking the Bailong River, submerging upstream hydropower stations, and damaging the S313 highway [8].

The problem of ancient landslide reactivation has been extensively studied by many scholars, both domestically and internationally. The main influencing factors include active faults and earthquakes, mechanical properties of weak interlayers within the accumulation body, changes in reservoir water levels, heavy rainfall, river erosion, and human engineering activity, etc. [11–16]. Among them, the relationship between ancient landslide reactivation and rainfall has attracted widespread attention. Most scholars have a significant opinion that there is a rainfall threshold for ancient landslide deformation instability, and usually infer the possibility of ancient landslide instability according to rainfall intensity [17–19]. Furthermore, they also point out that the rainfall thresholds in different regions and different types of landslides show significant differences [17–19]. For example, Gil and Długosz (2006) collected and analyzed meteorological data and ancient landslide data in the Flysch Carpathians area. The results indicated that there are significant differences in the rainfall thresholds for different types of ancient landslide reactivation, with lower rainfall thresholds for muddy ancient landslides compared to sandy ancient landslides [17]. In addition, some scholars have pointed out that various changes in the ancient landslide accumulation body caused by rainfall infiltration are also important factors in ancient landslide reactivation, such as increases in bulk density of ancient landslide rock–soil mass, the softening of the landslides' mechanical properties, and the increase in pore water pressure and groundwater levels [20–28]. For example, Borja and White (2010), based on theoretical and numerical analyses, revealed the trend of landslide accumulation deformation and failure under hydrological driving. They pointed out that rainfall leads to an increase in the saturation degree of the slope rock–soil mass, reducing its cohesive strength and weakening the frictional resistance of the sliding zone [22].

Although the connection between ancient landslide reactivation and rainfall has been extensively explained, little attention has been paid to the influence of the interaction between rainfall and cracks on ancient landslide reactivation. The cracks play a significant indicative role in the reactivation deformation trend and instability range of the next stage of ancient landslides. Existing studies have shown that, under rainfall conditions, the deformation and instability of ancient landslides have typical stress–permeability–damage coupling characteristics [29–31]. When no cracks have developed on an ancient landslide, the influence of rainfall on the ancient landslide is limited in depth and range [32–34]. However, when cracks have developed on the ancient landslide, rainfall has a significant controlling effect on the ancient landslide's reactivation [33,35,36]. Macroscopic deformations such as cracks are products of the evolutionary process of ancient landslide reactivation, and serve as important preferential pathways for rainwater infiltration. The coupling effect of rainfall and cracks makes significant contributions to the further deformation and instability of ancient landslides.

Currently, effective methods for evaluating landslide stability and studying the mechanisms of landslide instability include engineering geological analysis, physical modeling, and numerical simulation. The model tests of landslide are based on the similarity theory and consider the influence of internal and external factors on landslide stability, which can allow us to monitor the parameter variation of the model [37–39]. The model test has the characteristics of high efficiency, accuracy, and cost-effectiveness, and is widely used in the study of landslides' instability mechanisms, deformation, and movement processes [40–45].

In this study, the Woda landslide, located in the upper Jinsha River in the eastern edge of the Qinghai–Tibet Plateau, is taken as a case study. Through landslide model tests, the deformation and failure patterns of the model slope, with and without cracks, under rainfall are studied, and the influence of cracks on the reactivation mechanism of an ancient landslide is revealed. The research results contribute to our understanding of the contribution of cracks to the reactivation mechanism of ancient landslides induced by

rainfall, as well as to predicting the deformation and failure patterns of ancient landslides. The results also provide theoretical references for local geological disaster prevention and mitigation efforts.

2. Landslide Prototype

The Woda landslide is located at Woda Village, Yanbi Township, Jiangda County, Qamdo City, Tibet, China. It is situated on the right bank of the upper Jinsha River on the southeastern edge of the Qinghai–Tibet Plateau (Figure 1). The overall landform of the Woda landslide resembles a chair shape, with mountain ridges forming the boundaries on both sides (Figures 1 and 2). The main sliding direction is 30°, with a longitudinal length of about 2100 m and a transverse width of about 1660 m. The total area of the Woda landslide is estimated to be around 2.64 × 10^6 m^2, and the maximum height difference between the sliding outlet and the front edge of the Jinsha River is up to 247 m (Figure 3). The accumulation area of the Woda landslide has an area of about 1.32 × 10^6 m^2. The Woda landslide has two sliding zones, with burial depths of 15 m and 25.5 m, respectively [46]. Based on this information, it is estimated that the volume of the Woda landslide deposit is approximately 28.81 × 10^6 m^3, making it an extremely large, high-level landslide [46,47]. According to field investigations, the underlying bedrock of the Woda landslide is mainly composed of shale and carbonaceous shale, with strike angles ranging from 280° to 310° and dip angles of 25° to 30°. The main components of the accumulation are gravelly soil and residual slope material. The gravel content ranges from 30% to 45%, with particle sizes ranging from 20 cm to 50 cm, showing angular shapes and poor roundness. In the sliding outlet of the front edge of the Woda landslide, a sliding zone soil composed of gravelly clay was found. It had a thickness of about 50~75 cm, appeared grayish-green, and exhibited a soft-plastic to flowing-plastic state. The gravel content was approximately 13% to 25%, with particle sizes ranging from 2 mm to 20 mm, showing distinct angular shapes and relatively poor roundness.

Our field investigation found that the accumulation area of the Woda landslide is currently in a stage of overall reactivation, and its deformation can be divided into two distinct zones: Zone I, with intense deformation, and Zone II, with weak deformation. Zone I exhibits several localized sliding areas, down scarps, and tensile cracks (Figure 2). The localized sliding areas are located at the front edge of the Woda landslide and the rear part of the accumulation area. The tensile cracks and downs scarps are concentrated in the front part of the accumulation area, indicating the direction of reactivation deformation of the Woda landslide. The down scarps have a vertical displacement ranging from 30 cm to 120 cm and lengths ranging from 30 m to 230 m. The tensile cracks have lengths ranging from 20 m to 130 m, widths ranging from 10 cm to 30 cm, and depths ranging from 50 cm to 300 cm. Most of the down scarps and tension cracks are arranged in a circular arc, and the strike is roughly perpendicular to the main sliding direction of the landslide or at a large oblique angle. Zone II shows less pronounced deformation characteristics, with the development of four down scarps and one localized sliding area. Considering the deformation characteristics of the Woda landslide accumulation and the topographic features, the probability of overall sliding occurrence is much higher in Zone I than in Zone II. Because the sliding surface of the localized sliding area at the front edge of Zone I is located near the deep sliding zone, the upper accumulation area has a steep free surface. Based on this, it can be inferred that Zone I may experience destabilization and failure along the deep sliding zone, with an estimated volume of instability of approximately 17.83 × 10^6 m^3.

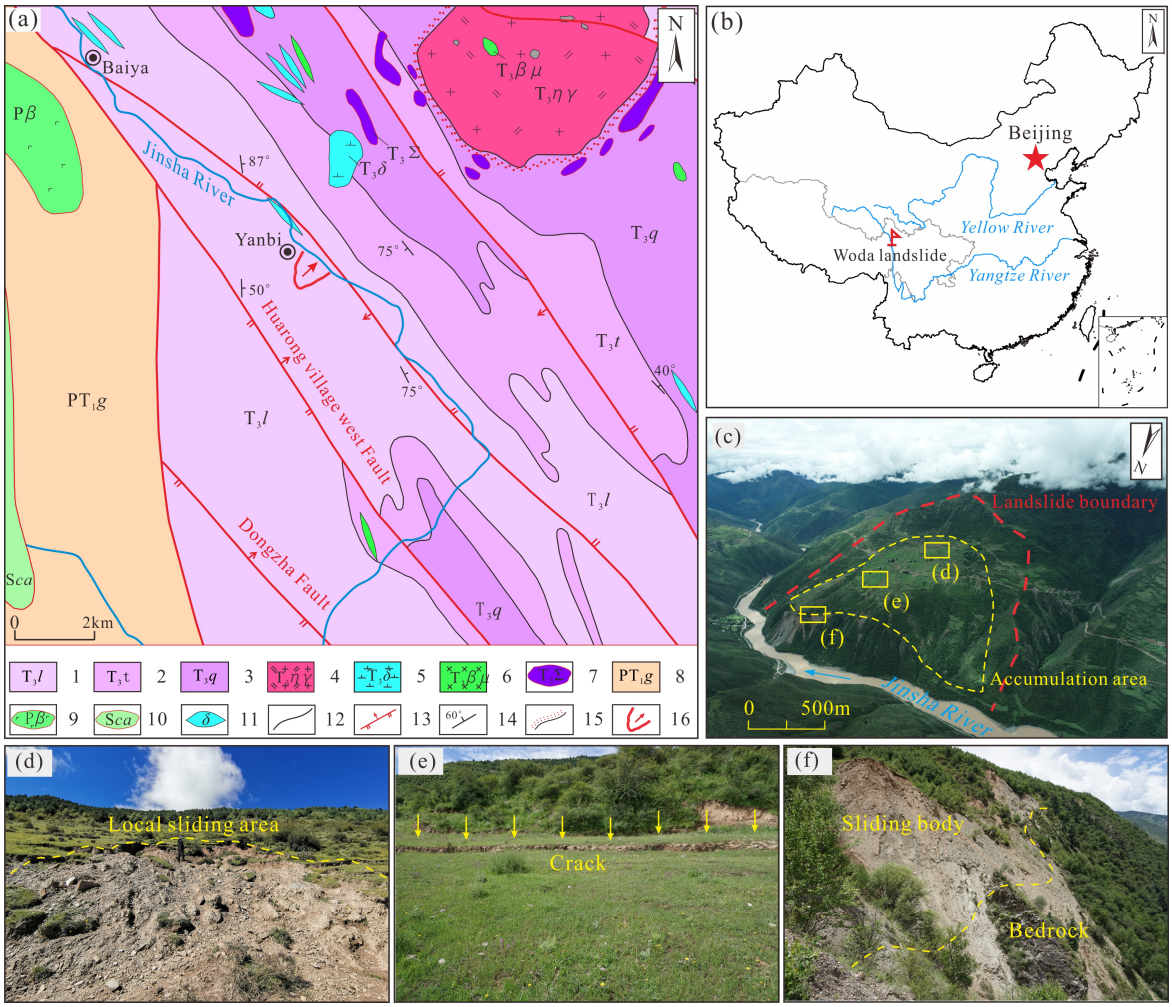

Figure 1. Geological setting of the Woda landslide (Modified according to Wu et al., 2023 [47]). (**a**) Tectonic and lithology map, (**b**) The Woda landslide location, (**c**) The Woda landslide panorama, (**d**) Local slide zone, (**e**) Tensile crack, (**f**) Leading edge shear outlet. 1—Schist, slate, shale in the Upper Triassic Lanashan Formation; 2—Crystal-line limestone, sandstone in the Upper Triassic Tumugou Formation; 3—Crystalline limestone in the Upper Triassic Qugasi Formation; 4—Monzonitic granites in the Upper Triassic; 5—diorite in the Upper Triassic; 6—dolerites in the Upper Triassic; 7—ultrabasic rocks in the Upper Triassic; 8—The sericite–quartz schist and the two-mica schist of the Gangtuoite Group in the Lower Permian-Triassic; 9—Basalt Blocks in the Permian; 10—Carbonate blocks in the Silurian; 11—Diorite dike; 12—Strata boundary; 13—Thrust fault; 14—Occurrence; 15—Hornfelsic zone; 16—The Woda landslide.

Wu et al. (2023) conducted a study indicating that the reactivation deformation rate of the Woda landslide is primarily controlled by the influence of seasonal rainfall [47]. Under the combined effects of rainfall infiltration and gravity, the slope deforms towards the downslope direction, resulting in the formation of down scarps and tensile cracks. These down scarps and tensile cracks serve as preferred infiltration pathways for rainfall, providing favorable conditions for the subsequent stage of deformation instability of the Woda landslide.

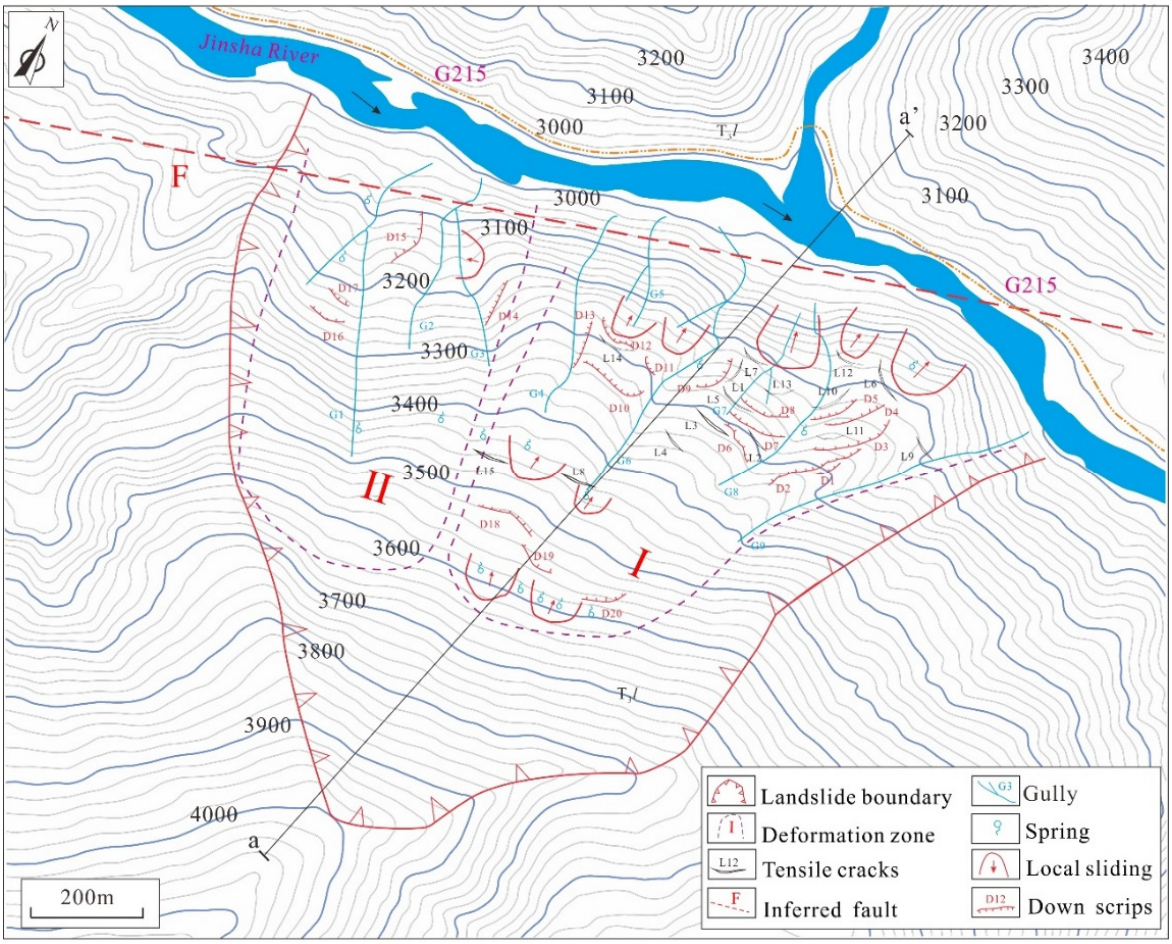

Figure 2. Engineering geological planar graph of the Woda landslide. I: intense deformation area, II: weak deformation area.

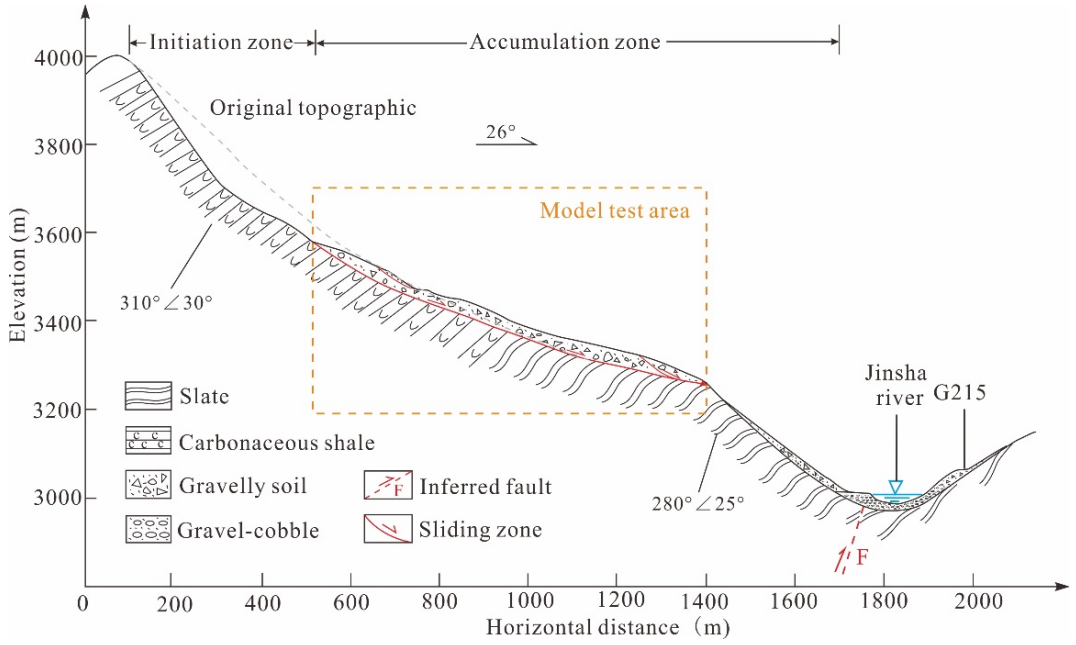

Figure 3. Engineering geological profile (a–a') of the Woda landslide.

3. Materials and Methods

3.1. Model Test Equipment

The model test was conducted in the Landslide Physical Model Laboratory of the Institute of Geomechanics, Chinese Academy of Geological Sciences. The main equipment of the landslide model test included a model box, rainfall simulation system, internal monitoring system, and slope surface monitoring system (Table 1 and Figure 4). With this comprehensive experimental setup, it was possible to monitor the real-time macro deformation and failure process of the physical model's slope surface, as well as pore water pressure and soil pressure inside the model slope under continuous rainfall conditions. The monitoring instruments and their key technical parameters used in this model test are shown in Table 1.

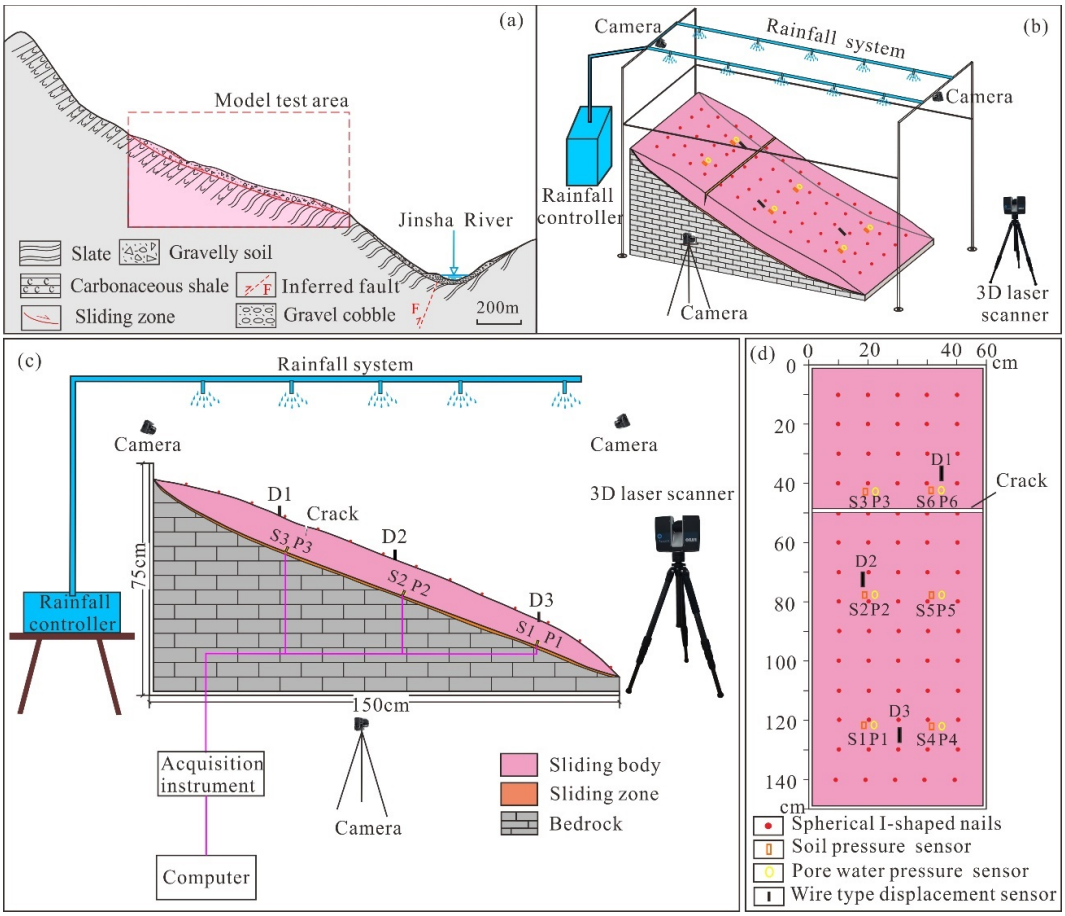

Figure 4. Equipment and instrument layout for the Woda landslide model test: (**a**) Model test area of the Woda landslide; (**b**) Three-dimensional view of the experimental model design effect; (**c**) Side view of the experimental model design effect; (**d**) Top view of the experimental model design effect.

3.2. Similar Materials

According to the similarity theory, the intense deformation Zone I of the Woda landslide was scaled down proportionally. The similarity ratio of 1:550 was determined based on the dimensions of the prototype and a physical model of the Woda landslide. A physical model was constructed based on the structural characteristics and potential unstable range of the Zone I in the Woda landslide. The model slope was divided into three parts: sliding body, sliding zone, and bedrock (Figure 4b,c). The dimensions of the model slope were approximately 165 cm in length, 60 cm in width, and 70 cm in height. The sliding zone had a thickness of about 2 cm, and the maximum thickness of the sliding body was 15 cm.

The similarity of the physical model to the Woda landslide was determined using dimensional analysis and similarity theory (Table 2). The main parameters of the similar

materials in the physical model included the geometric similarity ratio (l), density (ρ), moisture content (w), Poisson's ratio (μ), internal friction angle (φ), cohesion (c), displacement (δ), and permeability coefficient (k). Based on dimensional analysis and the homogeneity theorem, the above parameters can be expressed as follows:

$$f\ (l, \rho, w, \mu, \varphi, c, \delta, k) = 0$$

Table 1. Technical parameters of the model experimental instruments for the Woda landslide.

System Unit	Instruments	Model	Number	Key Technical Parameters
Model box	Model box	—	1	Size: 150 cm × 60 cm × 100 cm (length × width × height)
Rainfall simulation system	Atomizing nozzle	TW3010	5	Diameter: 0.3 mm; rainfall intensity: 0.063–0.251 mm/min.
	Atomizing nozzle	TW5010	5	Diameter: 0.5 mm; rainfall intensity: 0.163–0.433 mm/min.
	Water tank	—	1	Volume: 25 L
	Compressor	XK06-020	1	Rated voltage: 220 V; pressure: 0.5–3 MPa; volumetric flow rate of 0.032 m^3/min; output power: 0.55 kW
Internal monitoring system of the model	Soil pressure gauge	CYY2	6	Diameter: 6 mm; output voltage: 0–5 V; range: 0–4 kPa; accuracy: 0.01 kPa; dynamic frequency: 50 kHz
	Pore water pressure gauge	CYY9	6	Diameter: 6 mm; output voltage: 0–5 V; range: 0~2 kPa; accuracy: 0.01 kPa; dynamic frequency: 50 kHz
Model surface monitoring system	3D laser scanner	Faro S70	1	Scanning range: 0–360°; maximum scanning speed: 97 Hz; power consumption: 25 W; ranging error: <1 mm
	Camera	SONY-ILCE-6000	3	Sensor: Exmor APS-HD-CMOS; APS frame: 23.5 × 15.6 mm; maximum resolution: 6000 × 4000; optical zoom: 1–16 times
	Wire displacement meter	MPS-S	3	Range: 50–2000 mm; accuracy: 1 mm; tensile force: <600 g

Table 2. Similarity coefficient table for the model test of the Woda landslide.

Physical Quantity	Similarity Constant Code	Similarity Coefficient
Geometric dimensions, l	C_l	1:550
Density, ρ	C_ρ	1:1
Moisture content, w	C_w	1:1
Poisson's ratio, μ	C_μ	1:1
Internal friction angle, φ	C_φ	1:1
Cohesion, c	C_c	1:1
Displacement, δ	C_δ	1:550
Permeability coefficient, k	C_k	$1{:}550^{1/2}$

The bedrock of the physical model was simplified as impermeable or low-permeability bedrock, and was constructed by stacking bricks. A layer of cement mortar was applied onto the bedrock's top surface to achieve impermeability or low permeability. The selection and proportions of similar materials in the model were determined through comparative tests between multiple sets of similar material ratios and the prototype materials of the Woda landslide (sliding body and sliding zone) (Table 3). Among them, the sliding zone material consisted of gravel (2~5 mm), sand, bentonite, and water, with a ratio of 1:2:3:1.

The sliding body material consisted of gravel (5~10 mm), sand, heavy mineral powder (weighting material), silt, bentonite (binding material), and water, with a ratio of 1:2:8:9:3:3. Figure 5 shows the particle size distribution curves of the prototype and model materials of the Woda landslide, and Table 4 lists the physical and mechanical parameters of the prototype's and physical model's materials. In addition, to reduce the shear interaction between the side walls of the model box and the physical model of the landslide, Vaseline was uniformly applied to the contact area between the model box and the soil layer. The sensors were also positioned at a certain distance from the side walls of the model box (Figure 4d).

Table 3. Composition and proportion relationships between similar materials for the Woda landslide model test.

Material Type	Material Size (mm)	Material Proportion		Illustrate
		Sliding Zone	Sliding Body	
Gravel	2~5	1/6	-	
Sand	1~0.5	2/6	-	
Bentonite	<0.002	3/6	3/26	Binding material
Water	-	1/6	3/26	
Gravel	5–10	-	1/26	
Sand	0.2–2	-	2/26	
Barite powder	0.05–0.2	-	8/26	Weighting material
Silt soil	0.05–0.2	-	9/26	

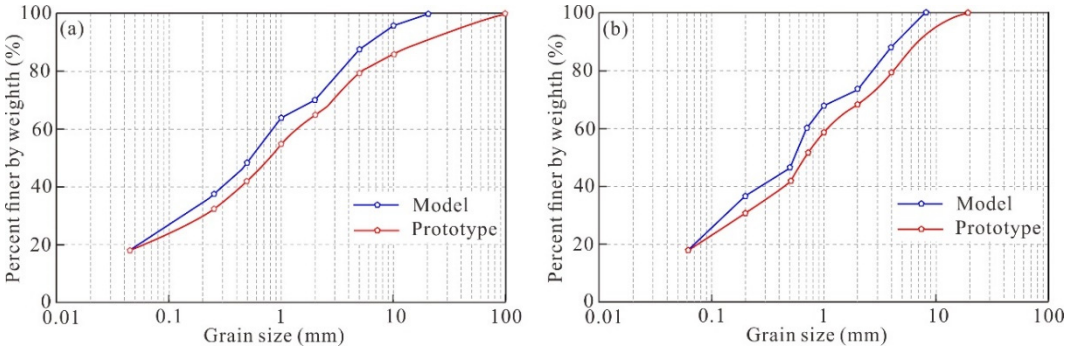

Figure 5. Particle size distribution curves of prototype and model materials: (**a**) Sliding body; (**b**) Sliding zone.

Table 4. Physical and mechanical parameters of the Woda landslide prototype materials and model materials.

Material Type		Density ρ (g/cm^3)	Moisture Content w (%)	Cohesion c (kPa)	Internal Friction Angle φ (°)	Permeability Coefficient k (m/s)	Volumetric Weight γ (kN/m^3)
Sliding body	Prototype	2.25	12	71.14	21.35	4.44×10^{-5}	22.05
	Model	2.24	12	63.34	22.62	1.92×10^{-6}	22.34
Sliding zone	Prototype	2.20	19	12.06	21.16	3.57×10^{-6}	21.56
	Model	2.21	19	10.14	20.06	1.51×10^{-7}	21.93

3.3. Test Conditions

Due to long-term geological evolution processes, the accumulation of an ancient landslide forms a gentle slope, and the internal body of the slope becomes compacted. The rock–soil mass has good cementing property and low permeability, making it more stable [30,36]. The shear outlet at the front edge of the Woda landslide is exposed, and the slope of the accumulation body is about 23°~25°, which has good deformation potential.

Under the infiltration of rainfall, tensile cracks gradually appear on the slope's surface. Under the action of gravity, rainwater infiltrates into the deep part of the slope along the cracks. This process promotes the development of cracks, which have wide upper parts and a narrow lower parts, resembling a "V" shape. Field investigations indicated that the tensile cracks in the intense-deformation Zone I of the Woda landslide did not penetrate the accumulation body.

In order to elucidate the evolution of the rainfall-induced deformation and destruction process of the Woda landslide, and to reveal the destabilization mechanism of the Woda landslide under the coupling effect of cracks and rainfall, two physical models of the landslide were created in this study (Table 5): (1) a physical model without cracks (Figure 6a), and (2) a physical model with a "V"-shaped crack at the rear edge, with 3 cm in top width, 7 cm in depth, and 60 cm in length (Figure 6b). Previous studies have indicated that rainfall intensity has a significant impact on the stability of ancient landslides [12,14,48]. To realistically reflect the influence of rainfall on the reactivation and deformation of the Woda landslide, meteorological data were collected, revealing that the monthly maximum rainfall in the study area is about 167 mm (Figure 6c), and the maximum daily rainfall is about 49.8 mm (Figure 6d). Combining with the similarity theory, the rainfall intensity in the model test was determined to be 7.02 mm/h, corresponding to a rainfall intensity of 50 mm/d in the real environment. The model test was conducted under continuous rainfall during the test period (Figure 6e). Because rainfall has a certain negative influence on data collected by 3D laser scanners and cameras, we stopped the rainfall and collected data for some important time nodes, such as local sliding and crack expansion, during the model tests.

Table 5. Experimental conditions of landslide model tests.

Scenario	Test Conditions	Rainfall Intensity (mm/h)	Crack Location	Crack Geometry Parameter
Scenario 1	Rainfall	7.02	-	-
Scenario 2	Coupling effect of rainfall and crack		Model trailing edge	V-shaped, 3 cm in width, 7 cm in height, 60 cm in length

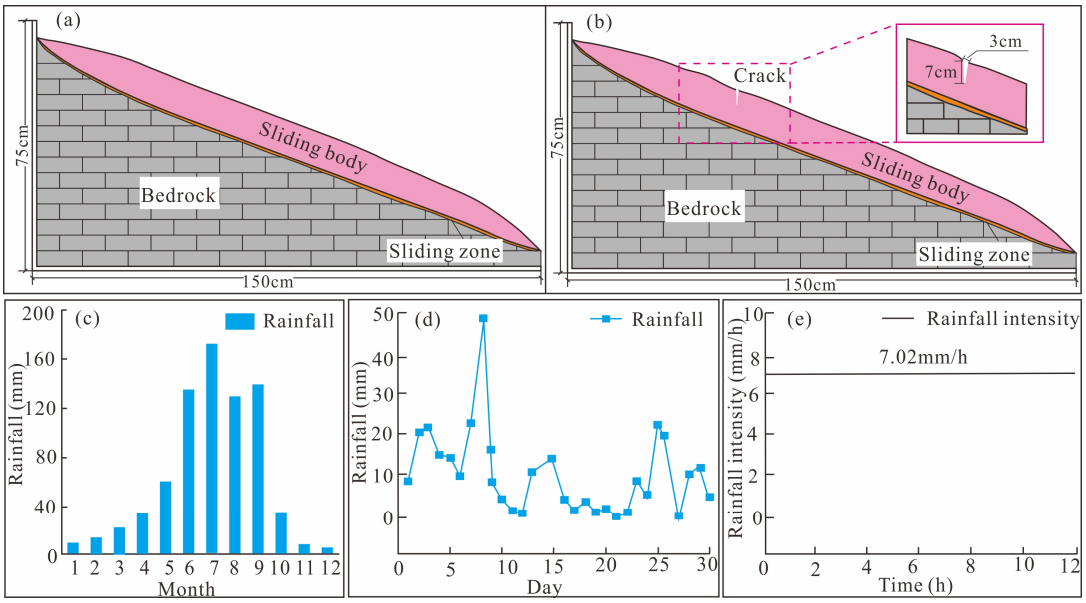

Figure 6. Physical model setup and rainfall schedule for the Woda landslide: (**a**) Model 1; (**b**) Model 2. (**c**) Monthly rainfall in the study area (2018); (**d**) Daily rainfall in the study area (July 2020); (**e**) Continuous rainfall process.

3.4. Instrument Layout

During the model test, three cameras and one 3D laser scanner were utilized to obtain the surface deformation characteristics of the physical model. The application of 3D laser scanning technology enables rapid acquisition of high-precision and high-resolution topographic data in the field, which is of great significance for landslide deformation monitoring. It has been widely used in the deformation monitoring of landslides and other geological disasters, as well as in landslide model tests [49–52]. Small cylindrical nails with diameters of 1 cm were strategically positioned on the model surface as monitoring points, with an interval spacing of 10 cm. Prior to rainfall, the model was scanned to obtain its undeformed shape, which served as a reference for measuring the deformation of the model during the model test.

Additionally, three monitoring sections were established at the front, middle, and rear parts of the physical model to acquire response characteristics related to surface displacement, internal soil pressure, and pore water pressure. Each section was equipped with a displacement sensor installed on the model surface. Furthermore, three soil pressure sensors and pore water pressure sensors were placed on each side of the central axis at approximately 10 cm intervals. These sensors were installed near the interface between the sliding zone and the sliding body (as depicted in Figure 4c,d).

4. Results

4.1. Deformation Processes of Landslides

In the model test process of scenario 1, several phenomena were observed. Initially, settlement deformation was predominantly exhibited during the onset of rainfall. After approximately 178 min of continuous rainfall, a shallow surface collapse occurred at the foot of the slope (Figure 7c). Between 178 and 362 min, an arc-shaped expansion of the collapsed area took place at the foot of the slope, accompanied by non-uniform settlement in the middle section, where greater settlement was observed on the right side compared to the left side (Figures 7d and 8d). From 362 to 838 min, localized instability and subsequent backward expansion were experienced on the right side of the model's front edge, with a fan-shaped failure pattern evident within this region (Figure 7e). The maximum thickness of this instability zone reached approximately 5.49 cm (Figure 8e), while non-uniform settlement continued expanding on the right side of the slope. At around 1108 minutes into rainfall, complete collapse occurred along with failure of the entire front edge in the model (Figure 7f), reaching a maximum instability thickness close to 10.95 cm (Figure 8f). By minute 1300 of rainfall, no further signs of deformation were observed in the model, and thus, the model test was concluded.

In the model test process of scenario 2, several phenomena were observed. During the initial stage of rainfall, settlement deformation with a magnitude of approximately 2 mm primarily occurred in the model (Figures 9 and 10). From 112 to 220 min, localized sliding took place in the middle part of the model's front edge, resulting in a tongue-shaped morphology measuring approximately 35 cm in length and approximately 20 cm in width. Seven tensile cracks developed in the middle-rear part of the slope (Figure 9c), while four tensile cracks appeared at the rear edge of the slope. The main tensile crack, L_1, had a length of approximately 42 cm and a width of approximately 1 cm. On both sides of the L_1 tensile crack, three tensile cracks, $L_{1\text{-}1}$ to $L_{1\text{-}3}$, were distributed, measuring 4 to 20 cm in length and approximately 0.3 cm in width (Figure 9c_1). At 10 cm from the preset crack, three tensile cracks, L_2, L_3, and L_4, were formed in the middle part of the slope. The L_2 and L_3 tensile cracks were approximately 48 to 55 cm in length and 0.5 to 1 cm in width, while the L_4 tensile crack was approximately 23 cm in length and 0.3 cm in width (Figure 9c_2). During the period of 220 to 397 min, localized sliding at the front edge of the model intensified, and new two tensile cracks, L_5 and L_6, formed in the middle part of the slope. Tensile cracks L_2 to L_4, in the middle part of the slope, were basically connected laterally (Figure 9d). From 397 to 492 min, a larger-scale sliding occurred on the right side of the model, and the tensile cracks in the middle and rear parts of the slope further expanded (Figure 9e).

During the period of 492 to 556 min, the entire front edge of the model experienced sliding, and the rear part of the slope lost support. Tensile crack L_3 connected with L4; the slope located before them experienced a slide of approximately 0.5~1.5 cm, with a maximum instability thickness of approximately 10.4 cm (Figure 10e). From 556 to 653 min of rainfall, progressive failure occurred in the mid-rear area of the model. Failure of the model's middle sliding body occurred, which was located at front of the L_3 and L_4 tensile cracks (Figure 9f), leading to the sliding of the block in front of the L_2 crack at the rear of the model (Figure 9g), with a maximum instability thickness of approximately 15.2 cm (Figure 10f). By 660 min of rainfall, no new signs of deformation were observed in the model, and the model test was concluded.

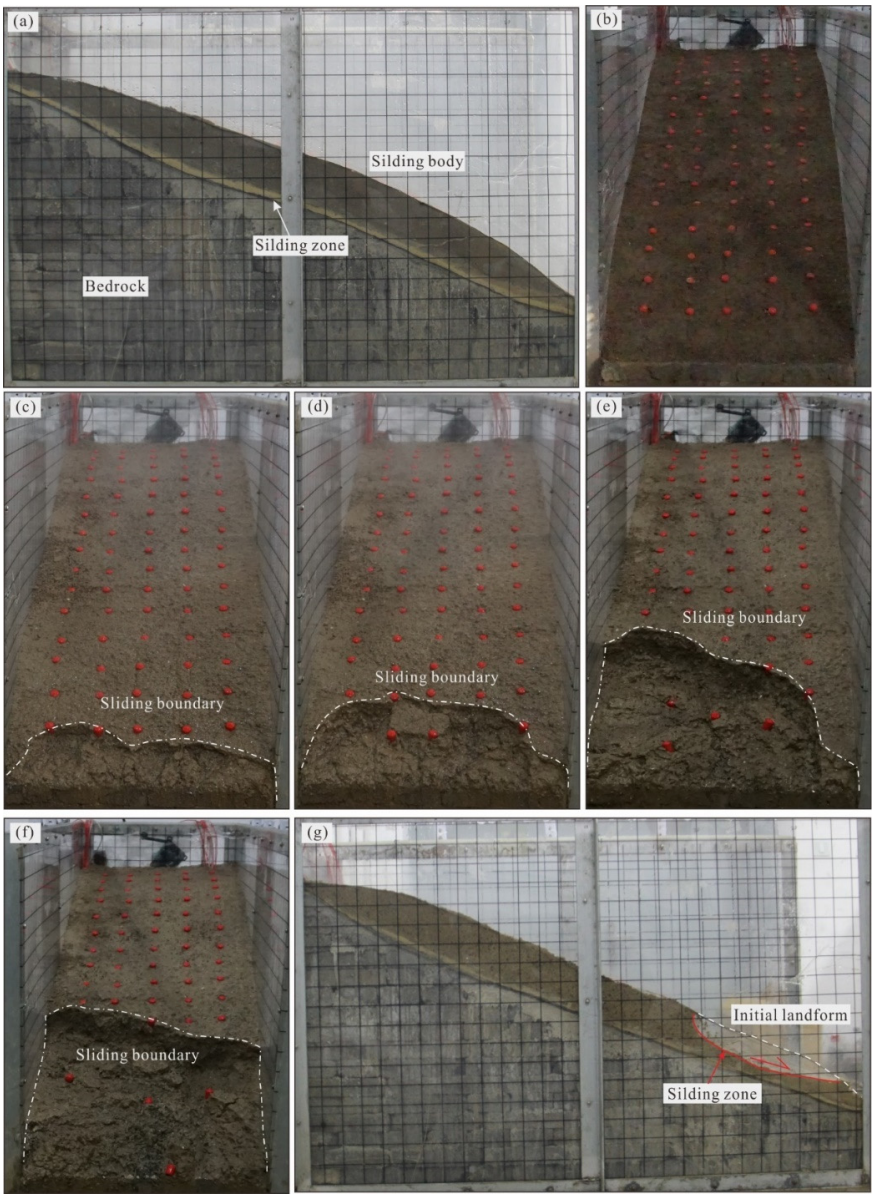

Figure 7. Deformation and failure characteristics of the model slope in different stages under working scenario 1: (**a**) Side view of the model slope, (**b**) Front view of the model slope, (**c**) Deformation and failure characteristics of the slope during the 0–178 min stage, (**d**) Deformation and failure characteristics of the slope during the 178~362 min stage, (**e**) Deformation and failure characteristics of the slope during the 362–838 min stage, (**f**) Deformation and failure characteristics of the slope during the 838~1108 min stage, (**g**) Deformation and failure characteristics of the slope during the 838~1108 min stage (side view).

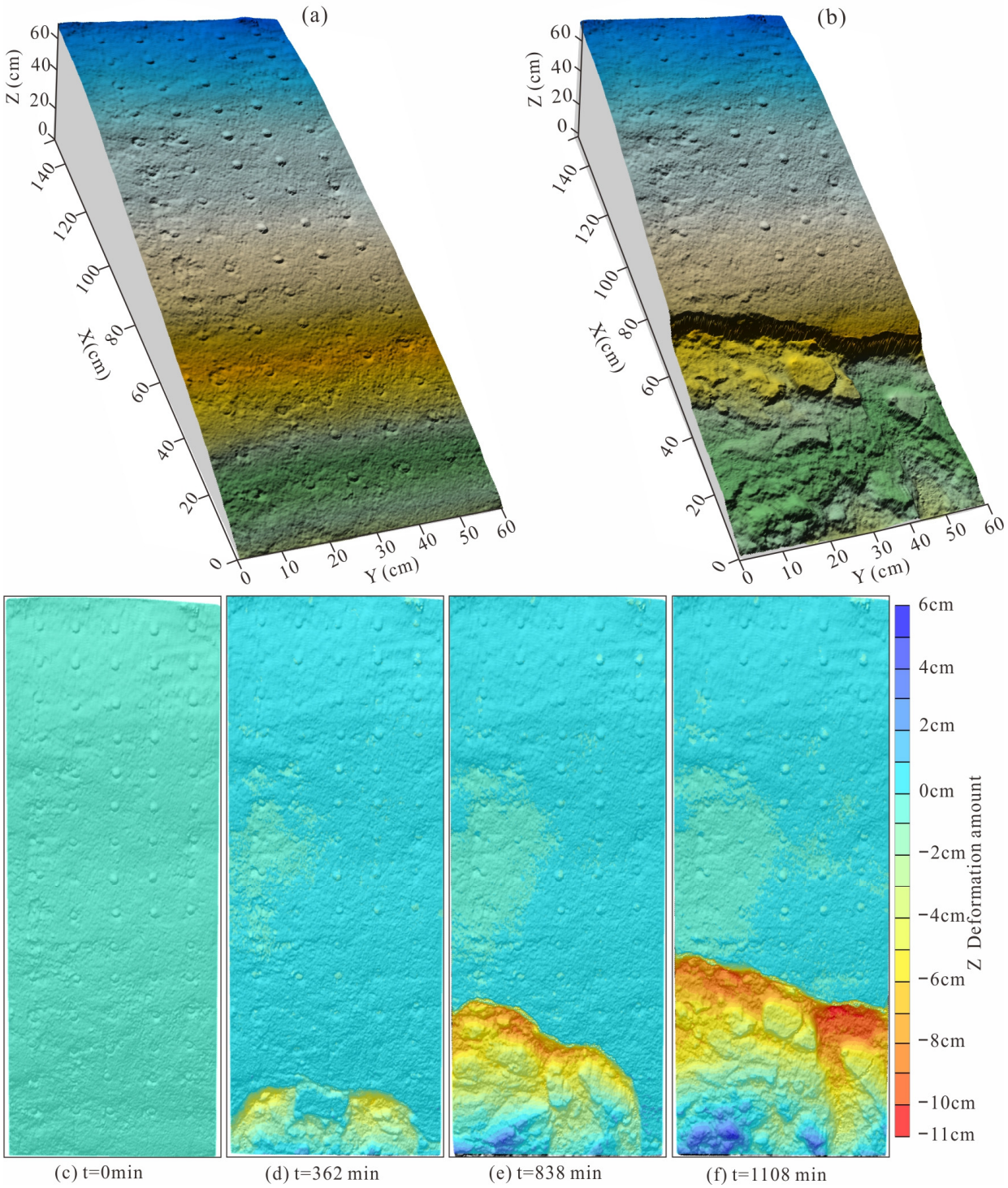

Figure 8. Orthophoto evolution of the landslide model test under working scenario 1: (**a**) Three-dimensional model slope before the model test; (**b**) Three-dimensional model slope after the model test; (**c–f**) Cloud maps in the Z-deformation amount of the slope at different times.

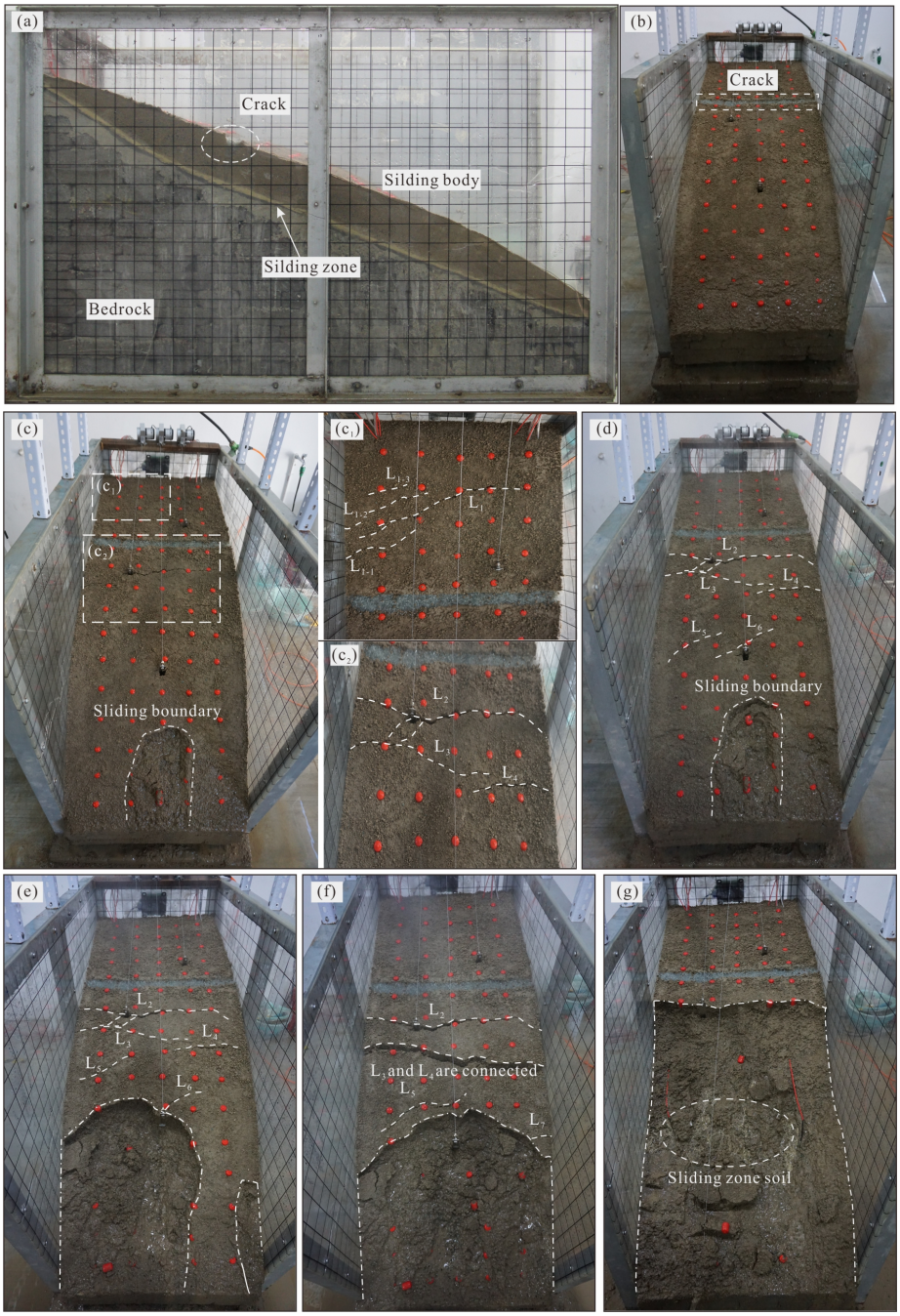

Figure 9. Deformation and failure characteristics of the model slope in different stages under working scenario 2: (**a**) Side view of the model slope; (**b**) Front view of the model slope; (**c**,**c$_1$**,**c$_2$**) Deformation characteristics of the slope body during the 112~220 min stage; (**d**) Deformation characteristics of the slope body during the 220~397 min stage; (**e**) Deformation characteristics of the slope body during the 397~492 min stage; (**f**) Deformation characteristics of the slope body during the 492~556 min stage; (**g**) Deformation characteristics of the slope body during the 556~653 min stage.

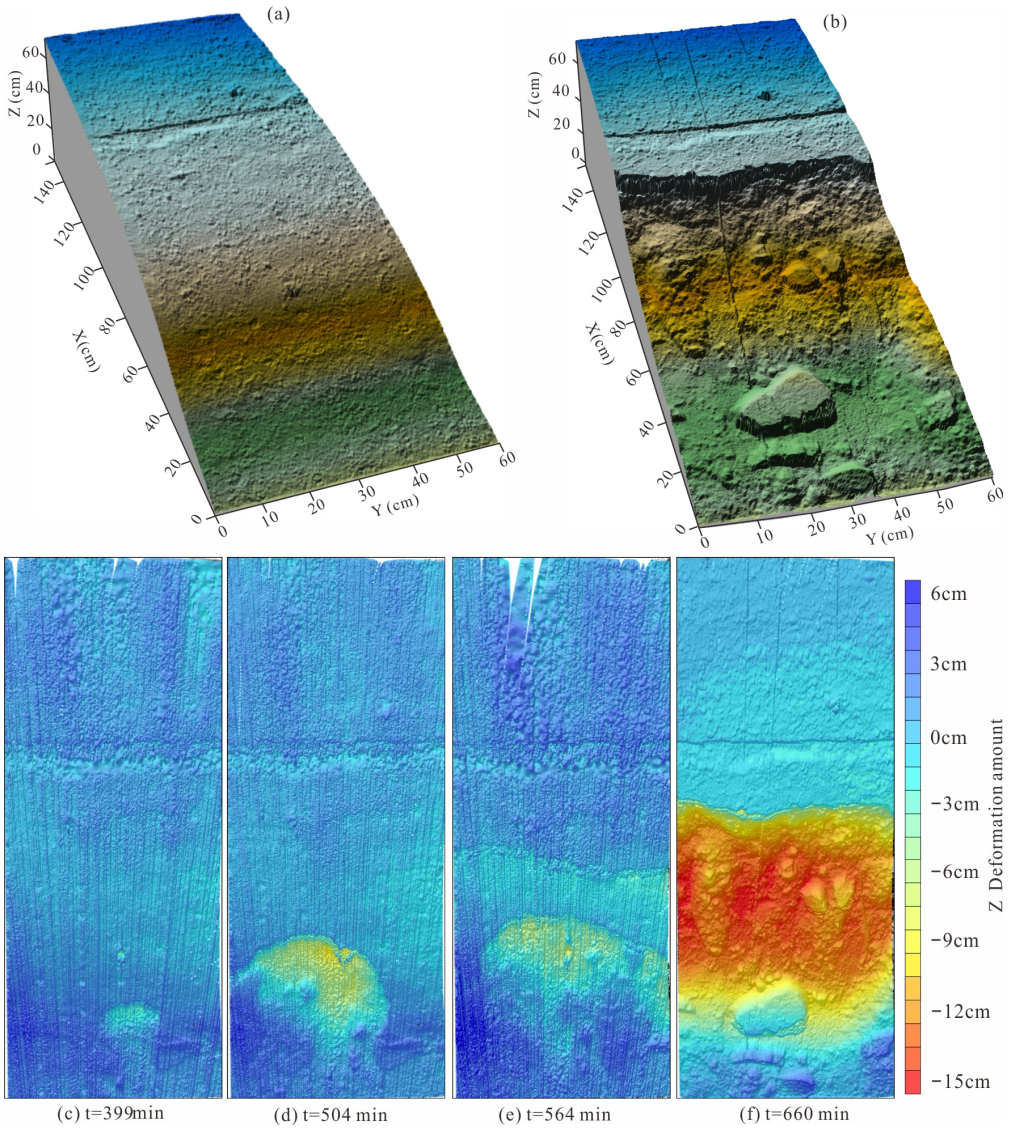

Figure 10. Evolution orthophotos of the model slope under working scenario 2. Evolution orthophotos of the model slope under working scenario 2: (**a**) Three-dimensional model slope before the model test; (**b**) Three-dimensional model slope after the model test; (**c**–**f**) Cloud maps of the Z-deformation of the model slope at different times.

4.2. Variation in Pore Water Pressure

In the model test process of scenario 1, a significant change in the pore water pressure at the mid-front of the model was observed. During the 0~100 min period of rainfall, the pore water pressure near the sliding zone in the slope was relatively low. At 105 min of rainfall, pore water pressure was first observed at monitoring point P4. The pore water pressure of P4 exhibited a transient sharp increase followed by a slow increase. At 248 min, the pore water pressure of P4 remained stable after a temporary reduction. From 130 to 435 min, there was a slow increase in pore water pressure at monitoring point P2. At 362~435 min, the pore water pressure of P4 rapidly raised after a temporary reduction. From 435 to 448 min, when the rainfall stopped, the pore water pressure of P2 and P4 continued to decrease. After 450 min, there was a sharp rise in pore water pressure at monitoring points P1 and P4. At time nodes 572 and 850 min, both P1 and P4 exhibited decreasing trends in pore water pressure, with decreases of 0.04 kPa, 0.07 kPa, 0.03 kPa, and 0.12 kPa, respectively. During the 950~975 min period, when the rainfall ceased, the pore water pressure decreased at all monitoring points at the mid-front of the model. Around 1108 min

of rainfall, there was a significant decrease in the pore water pressure at monitoring points P1, P2, P4, and P5, with reductions of 0.34 kPa, 0.02 kPa, 0.14 kPa, and 0.02 kPa, respectively. Throughout the entire model test, no pore water pressure was detected at monitoring points P3 or P6, which were located at the sliding zone on the rear edge of the slope (Figure 11).

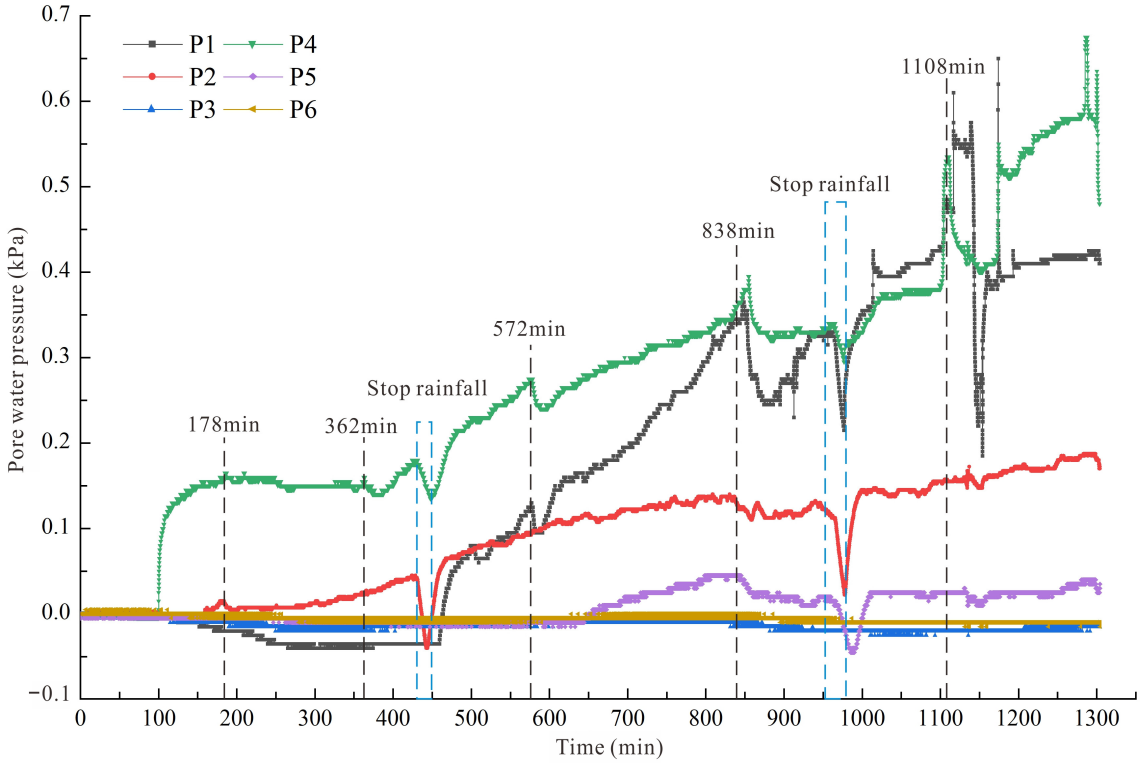

Figure 11. Process of pore water pressure changes under working scenario 1.

In the model test process of scenario 2, significant changes in the pore water pressure at all monitoring points of the model were observed. During the first 40 min of rainfall, there were no changes in pore water pressure. From 42 to 75 min, there was a sharp increase in the pore water pressure at five monitoring points, i.e., P5, P2, P4, P6, and P1, in order. From 104 to 158 min, except for monitoring point P3, the pore water pressure exhibited a transient decrease followed by another increase. At approximately 158 min, there was a sharp increase in the pore water pressure at monitoring point P3. From 175 to 187 min, when the rainfall stopped, the pore water pressure continued to decrease at all monitoring points. Around 220 min of rainfall, the pore water pressure decreased at all monitoring points, with the greatest reductions observed at monitoring points P1 and P3 on the right side of the slope. From 225 to 504 min, the pore water pressure slowly increased at all monitoring points, and at 490 min, the pore water pressure decreased again at all monitoring points. During the 504~520 min period of rainfall, there was a sudden increase followed by a sharp decrease in the pore water pressure at all monitoring points. From 510 to 525 min, when the rainfall ceased, the pore water pressure continued to decrease at all monitoring points. From 530 to 575 min, the pore water pressure at all monitoring points rose sharply and remained stable. There was a sudden drop in pore water pressure at monitoring point P4 at 560 min, while the remaining monitoring points showed a slowly decreasing trend. From 580 to 660 min, the pore water pressure initially increased slightly and then sharply decreased at all monitoring points. Pore water pressure reductions of 0.53 kPa, 1.09 kPa, 0.66 kPa, and 0.31 kPa were observed at monitoring points P1, P2, P4, and P5, respectively. The reductions in pore water pressure at monitoring points P3 and P6 were relatively small (Figure 12).

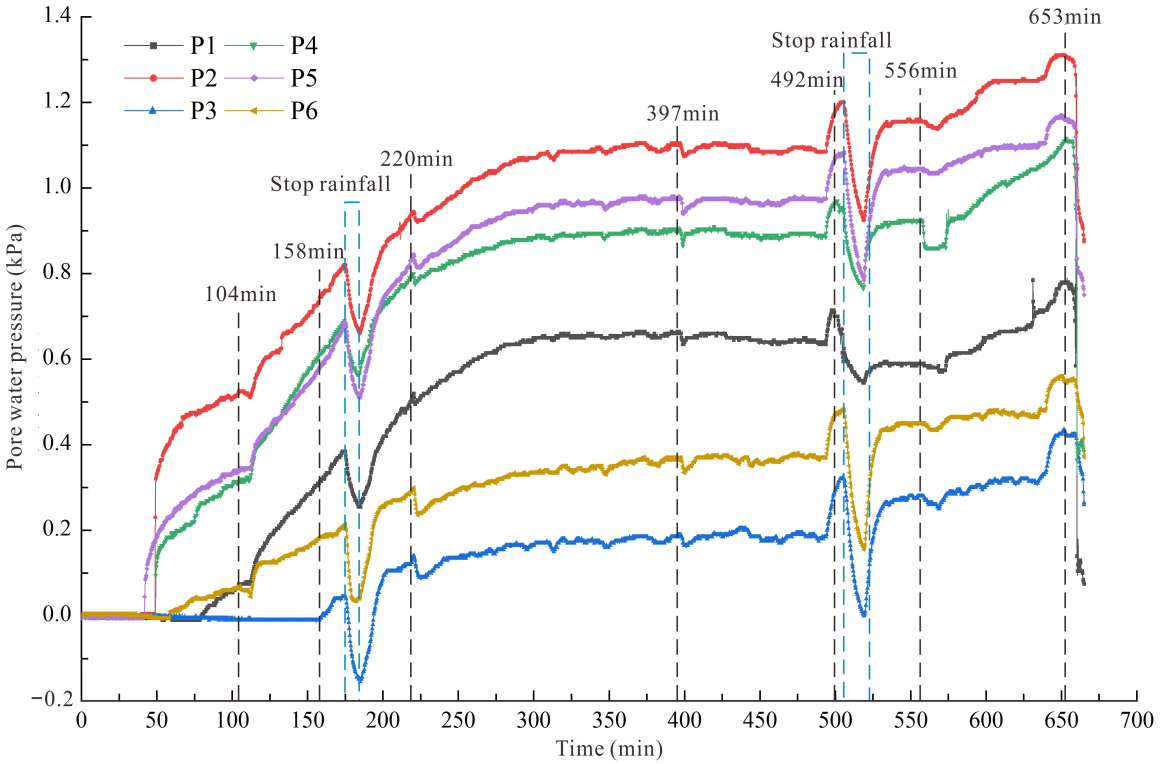

Figure 12. Process of pore water pressure changes under working scenario 2.

4.3. Variation in Soil Pressure

In the model test process of scenario 1, a significant change in soil pressure at the mid-front of the model was observed. During the 60 min before rainfall, the soil pressure at monitoring points S2 and S5 in the middle of the model gradually decreased and then sharply increased. The maximum soil pressures were 2.94 kPa and 1.98 kPa, respectively. Subsequently, during the model test, the soil pressures of S2 and S5 gradually decreased. From the 138th minute until the end of the model test, the soil pressure at monitoring point S6 slowly increased and exhibited oscillatory fluctuations, and the soil pressure at S3 remained stable throughout the process. From 38 to 150 min of rainfall, the soil pressures at S2 and S4 sharply increased and then slowly decreased. The maximum soil pressures reached were 2.46 kPa and 3.52 kPa, respectively. From 200 to 500 min, the soil pressures of S1 and S4 gradually increased, reaching peak values at the 342nd minute before slowly decreasing. From 500 to 830 min, the soil pressure at S1 remained constant, gradually increasing after the 742nd minute. The soil pressure of S4 gradually increased, experienced a sudden decrease at 595 min, increased again, reached its peak value after the 742nd minute, and remained stable thereafter. From 830 to 1108 min, the soil pressure at S1 continued to increase, reaching its peak value at the 950th minute and remaining stable. It then decreased in a stepped manner after the 1013th minute, and experienced a sharp decrease at the 1108th minute. The soil pressure at S4 briefly decreased, slowly increased, and rapidly decreased after the 1108th minute (Figure 13).

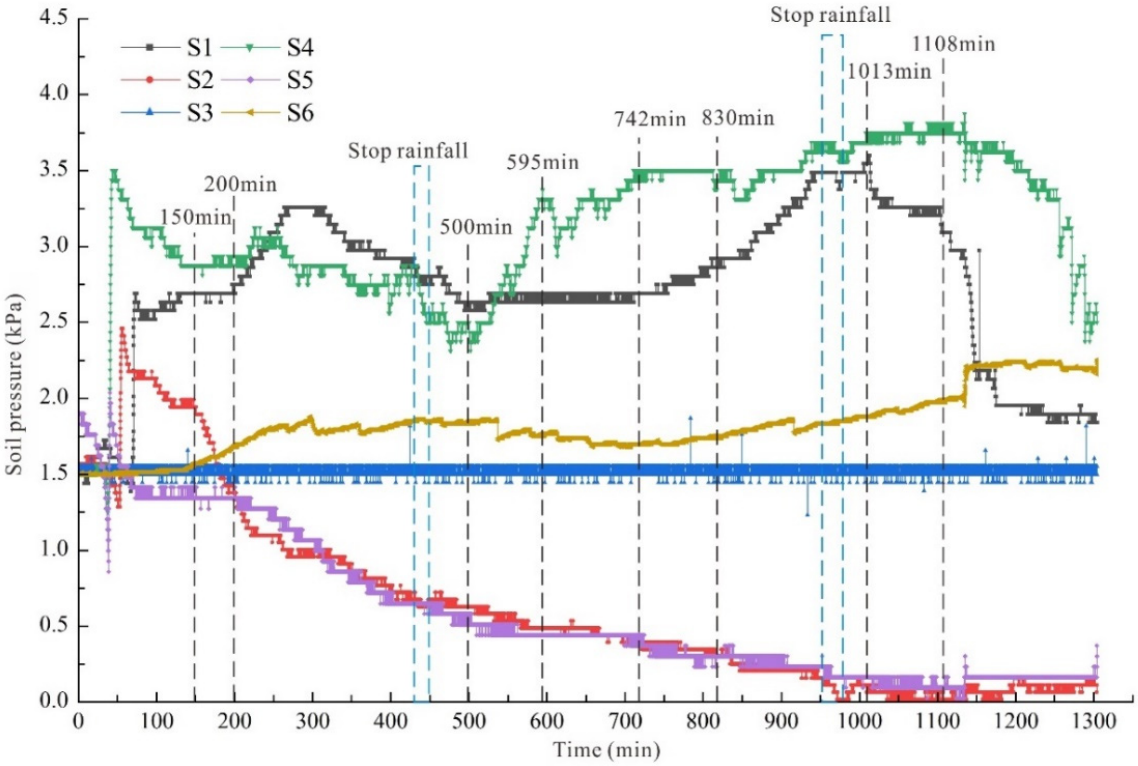

Figure 13. Monitoring curve of soil pressure under working scenario 1.

In the model test process of scenario 2, significant changes in soil pressure at all monitoring points were observed. At 0 to 104 min of rainfall, the soil pressure in the front part of the slope fluctuated intensively, while the rear crack area of the slope remained relatively stable. The soil pressure at monitoring point S3 remained unchanged, and the soil pressure at monitoring point S6 gradually increased and then stabilized until the end of the test. From 150 to 168 min, there was an increase, followed by a sudden drop in soil pressure at monitoring points S1 and S4. From 190 to 228 min, there was a brief increase followed by a decrease in soil pressure at monitoring points S1 and S4. From 228 to 400 min, the variation in soil pressure at all monitoring points was small during continuous rainfall. From 400 to 500 min, there was a slight decrease in the soil pressure at monitoring points S2 and S3 in the middle of the slope, while the soil pressure at S1 slowly increased. From 525 to 580 min, the soil pressure at monitoring points S1, S2, S4, S5, and other monitoring points slowly increased, followed by a gradual decrease in the soil pressure at monitoring point S4. From 580 to 650 min, there was a sudden increase followed by a sharp decrease in soil pressure at monitoring point S4 in the front left part of the slope, while the soil pressure at monitoring points S1, S2, S5, and others slowly increased and then gradually decreased (Figure 14).

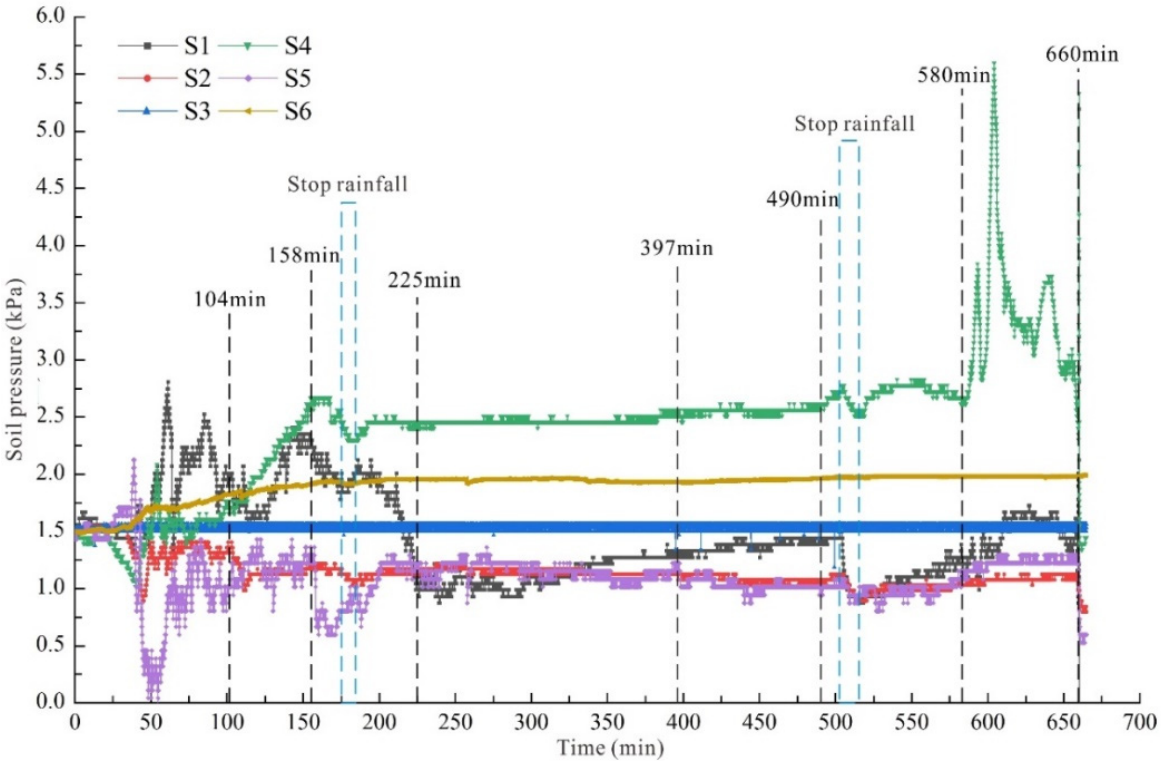

Figure 14. Monitoring curve of soil pressure under working scenario 2.

5. Discussion

5.1. The Mechanism of Ancient Landslide Reactivation

Under the action of rainfall, the reactivation mechanism of ancient landslides is closely related to cracks. When cracks develop on the slope's surface, surface water can rapidly infiltrate into the sliding zone along the preferential channels formed by the cracks [53]. This not only weakens the strength of the sliding zone soil, but also increases the groundwater and pore water pressure, thereby inducing ancient landslide reactivation [54,55]. The results of these model tests show that there are significant differences in the internal response characteristics of slopes with and without cracks. This leads to differences in the reactivation mechanisms of landslides under different conditions.

When a slope has no cracks, under the influence of gravity, rainwater rapidly accumulates at the foot of the slope. The saturation zone appears first at the foot of the slope, and it takes a relatively long time for rainfall to penetrate to the position of the sliding zone in the slope (at least 100 min). The pore water pressure at the front edge of the slope (P1 and P4) is greater than that at the middle and rear parts of the slope (P2 and P5, P3, and P6) (Figure 11). The results show that the influence of rainfall infiltration on the pore water pressure in the sliding zone of a slope occurs at the foot of the slope, the middle of the slope, and the back edge of the slope, in order. When a predetermined crack exists at the rear edge of the slope, the rainfall rapidly infiltrates into the deep part of the slope along the crack (about 50 min) and travels towards the middle and front edge under the influence of gravity, resulting in maximum pore water pressure at the middle part of the slope (P2 and P5), followed by the pore water pressure at the front edge of the slope (P1 and P4) and the minimum pore water pressure at the rear edge of the slope (P3 and P6) (Figure 12). The results show that the effect of rainfall infiltration on the pore water pressure in the sliding zones of cracked slopes is significantly different from that in slopes without cracks. In addition, the soil pressure at P3 on the right side of the rear edge of the landslide remained unchanged, and the soil pressure at P6 on the left side increased slowly, indicating that the rainfall quickly penetrated into the middle and lower parts of the slope after reaching the right side of the rear edge, while the water infiltration on the left side slowly led to

an increase in the body weight of the slope, which was consistent with the local slide first occurring on the right side of the slope.

Under rainfall conditions, the internal soil pressure response characteristics of slopes with and without cracks are significantly different. When a slope has no cracks, the maximum soil pressure is observed at the front edge (S1 and S4), followed by the rear edge (S3 and S6), and the minimum is found in the middle part (S2 and S5) (Figure 13). The soil pressure in the middle part (S2 and S5) continues to decrease, indicating that the influence from the rear edge gradually weakens in the middle part. This means that the rainfall's impact on the landslide is mainly concentrated in the middle and front parts. When the soil pressure in the middle part tends to stabilize, it indicates that there are no further signs of deformation in the rear edge of the slope. In addition, the soil pressure on the right side of the slope is less than that on the left side, which is consistent with the local sliding on the right side of the slope first. However, when predetermined cracks exist at the rear edge of the slope, the rainfall quickly affects the deep part of the slope along the crack and infiltrates into the middle and front parts of the slope. The soil pressure in the middle part fluctuates within a small range during the experimental process (Figure 14), indicating that the rear edge of the landslide continues to deform and pushes against the middle and front parts. As a result, the front part of the slope collapses and further triggers deformation and failure in the middle and rear parts, ultimately leading to overall instability of the landslide. The comparison between monitoring data and slope deformation and failure process shows that, before local sliding occurs, the soil pressure inside the slope increases abruptly for a short time and then decreases sharply after local sliding of the slope.

Based on the aforementioned analysis, solely considering rainfall conditions, significant disparities in reactivation mechanisms of slopes with and without cracks can be observed. When the slope had no cracks, the reactivation mechanism of the ancient landslide under rainfall primarily manifested as foot erosion and localized progressive failure at the front edge, with a limited impact range and depth (Figure 15a). However, when cracks existed on the slope, the mechanical behavior of the reactivation mechanism became complex. It exhibited mid-rear sliding body creeping, tensile cracks developed on the mid-rear sliding body, localized sliding at the front edge, extension of the tensile cracks in the mid-rear sliding body, extension of the local sliding range at the front edge, accelerated creeping in the mid-rear sliding body, and progressive failure of the mid-rear sliding body (Figure 15b). The presence of dominant seepage as crack channels promotes the evolution process of ancient landslide reactivation under the same rainfall conditions, causing an increased range of deformation and failure of ancient landslides.

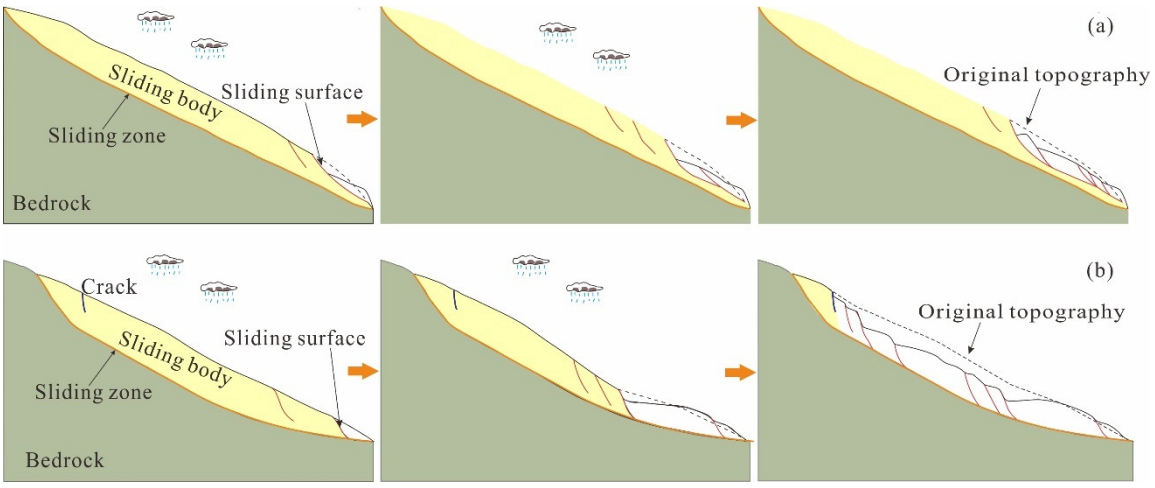

Figure 15. Reactivation mode of an ancient landslide with and without cracks: (**a**) Scenario 1, (**b**) Scenario 2.

5.2. The Evolution Process of Ancient Landslide

The model tests demonstrate that, under rainfall conditions, both slopes with and without cracks exhibit progressive retrogressive failure in terms of deformation and failure patterns. However, there are notable distinctions in the extent of failure. When there are no cracks in the slope, only the front edge of the slope body experiences local sliding before the landslide, followed by the extension of deformation and failure towards the rear. The concentrated deformation and failure range is located at the front edge of the slope, and the front edge of the slope does not slide along the predetermined sliding zone, but forms a new sliding zone at a certain depth inside the sliding body. When a crack is present at the rear part of the slope, the middle and rear parts of the slope firstly develop some tensile cracks, followed by local sliding at the front edge. Under continuous rainfall, the range of local sliding at the front edge further expands and the deformation in the middle and rear parts intensifies, resulting in overall reactivation along the predetermined sliding zone.

Based on the analysis of the experimental results, this study roughly divides the evolution process of ancient landslide reactivation into the following three stages.

Stage 1: Non-uniform settlement and crack formation stage (Figure 16a,b,e,f): After undergoing long-term geological transformation, the material composition and structural characteristics of ancient landslides exhibit high density, high cementation, low permeability, and heterogeneity [56]. During the initial stage of rainfall, water only affects the shallow surface of the slope. The heterogeneity on the plane leads to non-uniform settlement of the landslide, resulting in tensile stress near the boundary of the non-uniform settlement in the shallow layer of the slope. This provides favorable conditions for the generation of micro-cracks on the slope surface. Subsequently, rainwater infiltrates into the internal part of the slope along the micro-cracks, and the micro-cracks extend longitudinally and transversely, interconnecting with each other and eventually forming cracks.

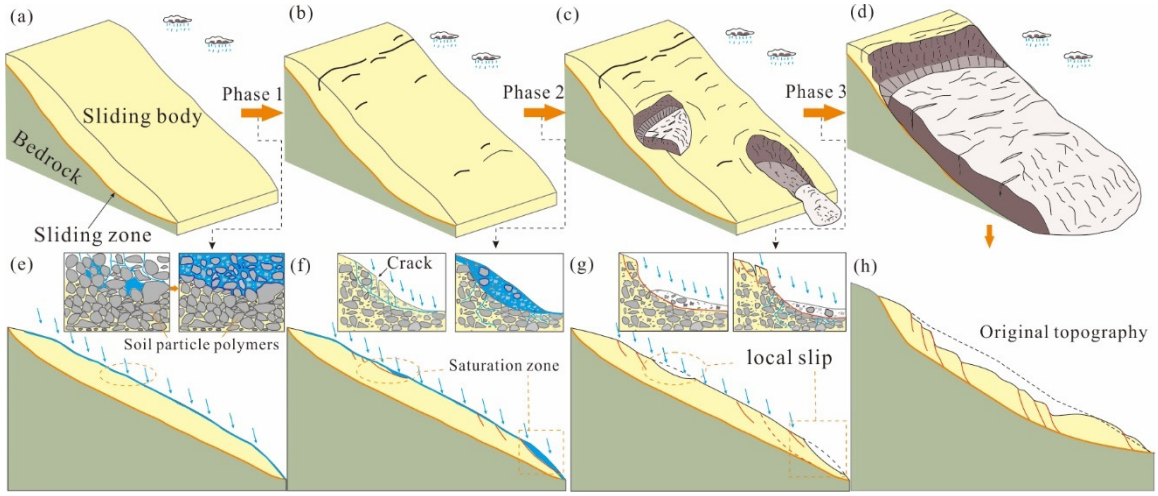

Figure 16. Evolution process of ancient landslide reactivation: (**a**) Initial model of ancient landslide; (**b**) Rainfall infiltration and crack formation on the slope surface; (**c**) Overall deformation and local sliding; (**d**) Progressive instability and failure; (**e**) Early stage of rainfall infiltration; (**f**) Process of flow channel formation; (**g**) Local sliding; (**h**) Progressive instability.

Stage 2: Crack extension and local sliding stage (Figure 16c,g): The crack in the shallow layer of the slope becomes the main preferential pathway for rainwater infiltration into the deep part of the slope in the later stage. Under the influence of gravity, rainwater gradually infiltrates into the deep part of the slope and towards the direction of the free face. This causes the cracks on the slope to gradually extend towards the deep part and the direction of the free face, gradually evolving into local weak structural planes. The sliding body undergoes creep deformation along these local weak structural planes towards the direction of the free face (Figure 16g). Influenced by the topography, relatively flat areas

such as the accumulation platform and the foot of the slope are prone to forming locally water-rich, saturated zones. As a result, the pore water pressure rises within the slope, reducing the shear resistance of the structural planes, eventually leading to localized sliding of the sliding body.

Stage 3: Progressive failure and overall instability stage (Figure 16d,h): After localized sliding occurs at the front and middle parts of the slope, a free face with a steeper slope is formed. The weak structural planes or sliding zones are exposed to the free face, developing a series of tensile cracks around the boundary of the localized sliding (Figure 16c). Rainwater quickly infiltrates along these tensile cracks to the slip bands, resulting in the degradation of the mechanical properties of the sliding zone and a significant reduction in shear resistance. The rear part of the slope undergoes accelerated creep deformation, and the cracks in the middle and rear parts extend, eventually leading to instability and failure. This evolutionary process is nearly identical to the process of excavation-induced instability of landslides, but the effects of water are slow. Rainfall-induced landslide deformation has characteristics such as multi-stage and multi-phase occurrence [37].

5.3. Limitations and Inspirations of Model Test

By analyzing the deformation and failure processes and the characteristics of model slopes with and without cracks under rainfall conditions, the reactivation mechanisms of ancient landslides under the influence of rainfall or the coupling effect between rainfall and cracks were revealed. However, this model test has certain limitations and is not sufficient for the evaluation of the hazard or stability of a landslide. The cracks in this model test were only considered in terms of depth and position, without considering factors such as the number of cracks, their extension lengths, or their directions. Therefore, they cannot truly reflect the current state of the landslide.

Currently, both our model test and numerical simulation are effective methods to evaluate landslide stability. Numerical simulation has been widely used due to its efficiency, convenience, accuracy, flexibility, and low cost [57,58]. In landslide engineering, the accuracy of stability evaluation results obtained through model tests and numerical simulations depends mainly on whether the evaluation models truly reflect the landslide prototype. Most researchers generalize the landslide prototype and ignore certain factors, such as slope body cracks, and establish generalized models based on the major factors for evaluation [57,59,60]. Although some results have been achieved through this approach, it also ignores the factors that influence the evaluation results, such as groundwater, cracks, etc. Based on the analysis of the results of this experimental study, for the evaluation of stability in ancient landslides, it is necessary to further consider the geometric characteristics of landslide cracks and their influences on stability, such as depth, width, length, and orientation.

6. Conclusions

In this study, the Woda landslide was taken as a case study, and the deformation and instability processes of different model slopes with and without cracks were investigated under rainfall conditions based on model tests. The influence of cracks on ancient landslide reactivation was analyzed, and the reactivation mechanism of ancient landslides under the coupling effect of rainfall and cracks was revealed. The following main conclusions are drawn:

1. The influence of rainfall on the deformation process, instability, and range of an ancient landslide is closely related to cracks. When there are no cracks in an ancient landslide, the deformation and failure of the ancient landslide are concentrated mainly in the front part, with the impact mainly limited to the shallow sliding body at the front part of the ancient landslide. However, when cracks develop on an ancient landslide, rainwater can rapidly infiltrate into the deep sliding zone along the cracks, resulting in overall deformation and instability of the ancient landslide.

2. Under rainfall conditions, significant differences can be observed in the response characteristics of pore water pressure and soil pressure in the deep parts of ancient landslides with and without cracks. When cracks develop on ancient landslides, the time required for rainwater to infiltrate into the deep sliding area is twice as long as in ancient landslides with cracks. Rainfall first causes changes in the pore water pressure and soil pressure at the foot of the ancient landslide, followed by the middle of the ancient landslide, with the least impact at the rear of the ancient landslide. When cracks develop on an ancient landslide, rainfall first causes changes in the pore water pressure and soil pressure at the mid-rear of the ancient landslide, followed by changes in the pore water pressure and soil pressure at the foot of the ancient landslide.
3. The reactivation mechanisms of ancient landslides under rainfall conditions and the coupling effect of rainfall and cracks show significant differences. In cases where there are no cracks present, the overall behavior involves erosion at the toe of the ancient landslide and progressive localized failure at the front edge, with the impact range and depth being limited. However, when cracks develop on ancient landslides, the mechanical behavior of the reactivation mechanism becomes more complex, including mid-rear ancient landslide creeping, tensile cracks developing at the mid-rear of the ancient landslide, localized sliding at the front edge, extension of tensile cracks, extension of the local sliding range, accelerated creeping, and progressive failure at the mid-rear of the ancient landslide.
4. Cracks play an important role in promoting the deformation and failure of ancient landslides. The characteristics of crack development in different stages of the reactivation of ancient landslides vary. It is recommended to consider the influence of crack development characteristics of ancient landslides, such as crack location, quantity, depth, length, and orientation, on their stability in the evaluation of landslide stability.

Author Contributions: X.L.: investigation, supervision, and writing—original draft. R.W.: conceptualization, methodology, formal analysis, and review. B.H.: supervision and review. D.S.: investigation, test, and data analysis. Z.W.: test and data processing. W.Z.: editing. Q.Z.: data processing. All authors have read and agreed to the published version of the manuscript.

Funding: This research was funded by National Key Research and Development Program of China, grant number [2021YFC3000505]; National Natural Science Foundation of China, grant number [42207233]; and China Geological Survey projects, grant number [DD20221816].

Data Availability Statement: Data are available on request from the authors.

Acknowledgments: The authors would like to thank Zhihua Yang, Jixin Liu, Ning Zhao, and Weiwei Shao for their help and support for performing the field investigation.

Conflicts of Interest: Author Deguang Song was employed by Yunnan Geological Engineering Second Survey Institute Co., Ltd. The remaining authors declare that the research was conducted in the absence of any commercial or financial relationships that could be construed as a potential conflict of interest.

References

1. Cruden, D.M.; Varnes, D.J. Landslide types and processes. In *Landslides: Investigation and Mitigation: Special Report 247*; Turner, A.K., Schuster, R.L., Eds.; National Academy Press: Washington, DC, USA, 1996; pp. 36–75.
2. Lu, Z.Y. Theory of landslide classification and sliding historical category. In Proceedings of the Sichuan Landslide Research and Prevention Experience Exchange Meeting, Chengdu, China, 1983.
3. Cruden, D.M.; Varnes, D.J. Landslide types and processes, special report, transportation research board. *Nat. Acad. Sci.* **1996**, *247*, 36–75.
4. Zhang, Y.S.; Guo, C.B.; Lan, H.X.; Zhou, N.J.; Yao, X. Reactivation mechanism of ancient giant landslides in the tectonically active zone: A case study in Southwest China. *Environ. Earth. Sci.* **2015**, *74*, 1719–1729. [CrossRef]
5. Li, Y.F.; Ji, Q.K. Short discussion on the distinction of paleo landslides. *West-China Explor. Eng.* **2006**, *128*, 287–296.
6. Zhang, M.S.; Li, T.L. Triggering factors and forming mechanism of loess landslides. *J. Eng. Geol.* **2011**, *19*, 530–540.

7. Iverson, R.M.; George, D.L.; Allstadt, K.; Reid, M.E.; Collins, B.D.; Vallance, J.W.; Schilling, S.P.; Godt, J.W.; Cannon, C.M.; Magirl, C.S.; et al. Landslide mobility and hazards: Implications of the 2014 Oso disaster. *Earth Planet. Sci. Lett.* **2015**, *412*, 197–208. [CrossRef]
8. Guo, C.B.; Zhang, Y.S.; Li, X.; Ren, S.S.; Yang, Z.H.; Wu, R.A.; Jin, J.J. Reactivation of giant Jiangdingya paleo landslide in Zhouqu County, Gansu Province, China. *Landslides* **2019**, *17*, 179–190. [CrossRef]
9. Notti, D.; Wrzesniak, A.; Dematteis, N.; Lollino, P.; Fazio, N.L.; Zucca, F.; Giordan, D. A multidisciplinary investigation of deep-seated landslide reactivation triggered by an extreme rainfall event: A case study of the Monesi di Mendatica landslide, Ligurian Alps. *Landslides* **2021**, *18*, 2341–2365. [CrossRef]
10. Macciotta, R.; Hendry, M.; Martin, C.D. Developing an early warning system for a very slow landslide based on displacement monitoring. *Nat. Hazards.* **2016**, *81*, 887–907. [CrossRef]
11. Muller, L. New Considerations on the Vaiont Slide. *Rock Mech. Eng. Geol.* **1968**, *6*, 1–91.
12. Liu, G.; Tong, F.G.; Zhao, Y.T.; Tian, B. A force transfer mechanism for triggering landslides during rainfall infiltration. *J. Mt. Sci.* **2018**, *15*, 2480–2491. [CrossRef]
13. Hu, X.W.; Huang, R.Q.; Zhu, H.Y.; Lv, X.P.; Zhang, X.; Shi, Y.B. Earthquake reactivation effects and stability study of malingyan landslide in Tangjiashan dammed lake. *Chin. J. Rock Mech. Eng.* **2009**, *28*, 1270–1278.
14. Guo, C.B.; Yan, Y.Q.; Zhang, Y.S.; Wu, R.A.; Yang, Z.H.; Li, X.; Ren, S.S.; Zhang, Y.Y.; Wu, Z.K.; Liu, J.X. Research Progress and Prospect of the Failure Mechanism of Large Deep-seated Creeping Landslides in the Tibetan Plateau, China. *Earth Sci.* **2022**, *47*, 3677–3700. Available online: https://kns.cnki.net/kcms/detail/42.1874.P.20220808.1553.020.html (accessed on 14 January 2024).
15. Yang, Y.T.; Dai, Z.W.; Lu, Y.S.; Zhang, C.Y.; Yan, H.; Hou, X.F.; Tang, J. Deformation characteristics and stability changes characteristics of reservoir landslides with double-sliding zones. *Earth Sci.* **2022**, 1–15. Available online: https://kns.cnki.net/kcms/detail/42.1874.P.20220809.1707.013.html (accessed on 14 January 2024).
16. Deng, L.X.; Xu, S.G.; Zheng, T.; Wu, J.; He, S.L. Analysis on the Reactivation Deformation Characteristics and Stability of Paleolandslide in Yongshan County. *Sci. Tech. Eng.* **2023**, *23*, 2308–2316.
17. Govi, M.; Sorzana, P.; Tropeano, D. Landslide mapping as evidence of extreme regional events. *Stud. Geomorphol Carpatho-Balc.* **1982**, *15*, 81–98.
18. Giannecchini, R. Rainfall triggering soil slips in the southern Aquan Alps. *Adv. Geosci.* **2005**, *2*, 21–24. [CrossRef]
19. Gil, E.; Długoszm, M. Threshold values of rainfalls triggering selected deep-seated landslides in the polish Flysch Carpathians. *Stud. Geomorphol Carpatho-Balc.* **2006**, *40*, 21–43.
20. De Vita, P.; Reichenbach, P.; Bathurst, J.C.; Marco, B.; Crosta, G.; Crozier, M.; Glade, T.; Guzzetti, F.; Hansen, A.; Wasowski, J. Rainfall-triggered landslides: A reference list. *Environ. Geol.* **1998**, *35*, 219–233. [CrossRef]
21. Iverson, R.M. Landslide triggering by rain infiltration. *Water Resour. Res.* **2000**, *36*, 1897–1910. [CrossRef]
22. Borja, R.I.; White, J.A. Continuum deformation and stability analyses of a steep hillside slope under rainfall infiltration. *Acta Geotech.* **2010**, *5*, 1–14. [CrossRef]
23. Borja, R.I.; White, J.A.; Liu, X.; Wu, W. Factor of safety in a partially saturated slope inferred from hydro-mechanical continuum modeling. *Int. J. Numer. Anal. Methods Geomech.* **2012**, *36*, 236–248. [CrossRef]
24. Cojean, R.; Cai, Y.J. Analysis and modeling of slope stability in the Three-Gorges Dam reservoir (China)—The case of Huangtupo landslide. *J. Mt. Sci.* **2011**, *8*, 166–175. [CrossRef]
25. Lee, Y.F.; Chi, Y.Y. Rainfall-induced landslide risk at Lushan. Taiwan. *Eng. Geol.* **2011**, *123*, 113–121. [CrossRef]
26. Qi, S.; Vanapalli, S.K. Computers and Geotechnics Influence of swelling behavior on the stability of an infinite unsaturated expansive soil slope. *Comput. Geotech.* **2016**, *76*, 154–169. [CrossRef]
27. Zhou, J.W.; Cui, P.; Hao, M.H. Comprehensive analyses of the initiation and entrainment processes of the 2000 Yigong catastrophic landslide in Tibet, China. *Landslides* **2016**, *13*, 39–54. [CrossRef]
28. Chen, M.L.; Lv, P.F.; Zhang, S.L.; Zhou, J.W.; Chen, M.L.; Chen, X.Z. Time evolution and spatial accumulation of progressive failure for Xinhua slope in the Dagangshan reservoir, Southwest China. *Landslides* **2018**, *15*, 565–580. [CrossRef]
29. Li, S.H.; Wang, Y.N. Selection study of computational parameters for DEM in geomechanics. *Chin. J. Rock Mech. Eng.* **2004**, *23*, 3642–3651.
30. Wang, Y.; Li, X.; He, J.M.; Wu, Y.F.; Wu, Y.S. Research status and prospect of rock and soil aggregate. *J. Eng. Geol.* **2014**, *22*, 112–123. [CrossRef]
31. Hu, F.; Li, Z.Q.; Hu, R.L.; Zhou, Y.X.; Yuan, R.Q. Research on the deformation characteristics of shear band of soil-rock mixture based on large scale direct shear test. *Chin. J. Rock Mech. Eng.* **2018**, *37*, 766–778. [CrossRef]
32. Li, A.G.; Yue, Z.Q.; Tham, L.G.; Li, A.G.; Law, K.T. Field-monitored variations of soil moisture and matric suction in a saprolite slope. *Can. Geotech. J.* **2005**, *42*, 13–26. [CrossRef]
33. Li, T.L.; Xi, Y.; Hou, X.K. Mechanism of surface water infiltration induced deep loess landslide. *J. Eng. Geol.* **2018**, *26*, 1113–1120. [CrossRef]
34. Hu, R.L.; Lc, X.; Wang, Y.; Gao, W.; Xia, J.G.; Li, Z.Q.; Gao, W.W.; Sun, Y.S. Research on engineering geomechanics and structural effect of soil-rock mixture. *J. Eng. Geol.* **2020**, *28*, 255–281. [CrossRef]
35. Zhou, Z.; Shen, J.h.; Li, Y.; Duan, W.F.; Yang, R.C.; Shu, J.C.; Li, H.W.; Tao, S.Y.; Zheng, S.Z. Mechanism of colluvial landslide induction by rainfall and slope construction: A case study. *J. Mt. Sci.* **2021**, *18*, 1013–1033. [CrossRef]

36. Zhang, Y.S.; Wu, R.A.; Ren, S.S. Influence of rainfall preponderance infiltration path on reactivation of ancient landslides. *Chin. J. Rock Mech. Eng.* **2021**, *40*, 777–789. [CrossRef]
37. Take, W.A.; Bolton, M.D.; Wong, P.C.P.; Yeung, F.J. Evaluation of landslide triggering mechanisms in model fill slopes. *Landslides* **2004**, *1*, 173–184. [CrossRef]
38. Rahardjo, H.; Lee, T.; Leong, E.C.; Rezaur, R. Response of a residual soil slope to rainfall. *Can. Geotech. J.* **2005**, *42*, 340–351. [CrossRef]
39. Luo, X.Q.; Liu, D.F.; Wu, J.; Cheng, S.G.; Sheng, H.; Xu, K.X.; Huang, X.B. Model test study on landslide under rainfall and reservoir water fluctuation. *Chin. J. Rock Mech. Eng.* **2005**, *24*, 2476–2483.
40. Jia, G.W.; Zhan, T.L.T.; Chen, Y.M.; Fredlund, D.G. Performance of a large-scale slope model subjected to rising and lowering water levels. *Eng. Geol.* **2009**, *106*, 92–103. [CrossRef]
41. Lin, M.L.; Wang, K.L. Seismic slope behavior in a large-scale shaking table model test. *Eng. Geol.* **2006**, *86*, 118–133. [CrossRef]
42. Moriwaki, H.; Inokuchi, T.; Hattanji, T.; Sassa, K.; Ochiai, H.; Wang, G. Failure processes in a full-scale landslide experiment using a rainfall simulator. *Landslides* **2004**, *1*, 277–288. [CrossRef]
43. Ochiai, H.; Okada, Y.; Furuya, G.; Okura, Y.; Matsui, T.; Sammori, T.; Terajima, T.; Sassa, K. A fluidized landslide on a natural slope by artificial rainfall. *Landslides* **2004**, *1*, 211–219. [CrossRef]
44. Rianna, G.; Pagano, L.; Urciuoli, G. Rainfall patterns triggering shallow flowslides in pyroclastic soils. *Eng. Geol.* **2014**, *174*, 22–35. [CrossRef]
45. Ma, J.W.; Tang, H.M.; Hu, X.L.; Bobet, A.; Yong, R.; Eldin, M.A.M.E. Model testing of the spatial–temporal evolution of a landslide failure. *Bull. Eng. Geol. Environ.* **2016**, *76*, 1–17. [CrossRef]
46. Wu, R.A.; Ma, H.S.; Zhang, J.C.; Yang, Z.H.; Li, X.; Ni, J.W.; Zhong, N. Developmental characteristics and damming river risk of the Woda landslide in the upper reaches of the Jinshajiang River. *Hydrogel. Eng. Geol.* **2021**, *48*, 120–128. [CrossRef]
47. Wu, R.A.; Yang, Z.H.; Guo, C.B.; Zhang, Y.S.; Song, D.G.; Ma, H.S.; Li, X.; Ni, J.W. Reactivation and dynamic process prediction of the Woda landslide in the upper Jinsha River Basin, China. *Environ. Earth Sci.* **2023**, *82*, 528. [CrossRef]
48. Ren, D.; Leslie, L.M.; Lynch, M.J.; Duan, Q.Y.; Dai, Y.J.; Wei, S.G. Why was the August 2010 Zhouqu landslide so powerful? *Georg. Environ.Sustain.* **2013**, *6*, 67–79. [CrossRef]
49. Abellan, A.; Vilaplana, J.M.; Martinez, J. Application of a long-range terrestrial laser scanner to a detailed rockfall study at Vall de Nuria (Eastern Pyrenees, Spain). *Eng. Geol.* **2006**, *88*, 136–148. [CrossRef]
50. Fanti, R.; Gigli, G.; Lombardi, L.; Tapete, D.; Canuti, P. Terrestrial laser scanning for rockfall stability analysis in the cultural heritage site of Pitigliano (Italy). *Landslides* **2013**, *10*, 409–420. [CrossRef]
51. Jaboyedoff, M.; Oppikofer, T.; Abellan, A.; Derron, M.H.; Loye, A.; Metzger, R.; Pedrazzini, A. Use of LIDAR in landslide investigations: A review. *Nat. Hazards.* **2012**, *61*, 5–28. [CrossRef]
52. Wang, G.Q.; Joyce, J.; Phillips, D.; Shrestha, R.; Carter, W. Delineating and defining the boundaries of an active landslide in the rainforest of Puerto Rico using a combination of airborne and terrestrial LIDAR data. *Landslides* **2013**, *10*, 503–513. [CrossRef]
53. Krzeminska, D.; Bogaard, T.; Malet, J.P.; van Beek, L.P.H. A model of hydrological and mechanical feedback of preferential fissure flow in a slow-moving landslide. *Hydrol. Earth Syst. Sci.* **2013**, *17*, 947–959. [CrossRef]
54. Lacroix, P.; Handwerger, A.L.; Bièvre, G. Life and death of slow-moving landslides. *Nat. Rev. Earth Environ.* **2020**, *1*, 404–419. [CrossRef]
55. Simoni, B.A. Observation and analysis of near-surface pore-pressure measurements in clayshales slopes. *Hydrol. Process.* **2012**, *26*, 2187–2205. [CrossRef]
56. Wang, R.B.; Wan, J.X.; Cheng, R.L.; Wang, Y.Z.; Wang, Z.Y. Physical and Numerical Simulation of the Mechanism Underpinning Accumulation Layer Deformation, Instability, and Movement Caused by Changing Reservoir Water Levels. *Water* **2023**, *15*, 1289. [CrossRef]
57. Zhang, X.; Tan, Z.Y.; Zhou, C.M. Seepage and stability analysis of landslide under the change of reservoir water levels. *Chin. J. Rock Mech. Eng.* **2016**, *35*, 713–723. [CrossRef]
58. Gu, T.F.; Wang, J.D.; Wang, N.Q. Geological features of loess landslide at Lüliang airport and its 3D stability analysis. *Rock Soil Mech.* **2013**, *34*, 2009–2016. [CrossRef]
59. Shen, T.; Wang, Y.S.; Huang, Z.Q.; Li, J.; Zhang, X.; Cao, W.Z.; Gu, J. Formation mechanism and movement processes of the Aizigou paleolandslide, Jinsha River, China. *Landslides* **2018**, *16*, 409–424. [CrossRef]
60. Shao, W.; Bogaard, T.A.; Bakker, M.; Greco, R. Quantification of the influence of preferential flow on slope stability using a numerical modelling approach. *Hydrol. Earth Syst. Sci.* **2015**, *19*, 2197–2212. [CrossRef]